

Asteroseismology of GD358 with complex C/O core profiles

Agnès Bischoff-Kim¹, J. L. Provencal^{2,3}, M. H. Montgomery^{3,4}, Samuel T. Harrold⁴, B. Howard³, W. Strickland⁵, D. Chandler⁵, D. Campbell⁵, A. Arredondo⁵, R. Linn⁵, D. P. Russell⁵, D. Doyle⁵, A. Brickhouse⁵, R. Linn⁵, D. Peters⁵, A. V. Kusakin⁶, A. V. Sergeev⁷, M. Andreev⁷, A. Maksim⁷, S. Velichko⁷, R. Janulis⁸, F. Aliçavuş⁹, N. Horoz⁹, S. Zola^{10,11}, W. Ogłóza^{10,11}, D. Koziel-Wierzbowska^{10,11}, T. Kundera^{10,11}, D. Jableka^{10,11}, B. Debski^{10,11}, S. Meingast¹²

ABSTRACT

We report on the analysis of 33 years of photometric observations of the pulsating helium atmosphere white dwarf GD358. The complete data set includes archival data from 1982-2006, and 1105.1 hours of new observations from 2007-2015. From this data set, we extract 15 frequencies representing g-mode pulsation modes, adding 4 modes to the 11 modes known previously. We present evidence that these 15 modes are $\ell = 1$ modes, 13 of which belong to a consecutive sequence in radial overtone k . We perform a detailed asteroseismic analysis using models

¹Penn State Worthington Scranton, Dunmore, PA 18512; axk55@psu.edu

²University of Delaware, Department of Physics and Astronomy Newark, DE 19716; jlp@udel.edu

³Delaware Asteroseismic Research Center, Mt. Cuba Observatory, Greenville, DE 19807

⁴Department of Astronomy, University of Texas, Austin, TX 78712; mikemon@rocky.as.utexas.edu

⁵Meyer Observatory and Central Texas Astronomical Society, 209 Paintbrush, Waco, TX 76705; chandler@vvm.com

⁶Fesenkov Astrophysical Institute, Almaty 050020, Kazakhstan

⁷Ukrainian National Academy of Sciences, Main Astronomical Observatory, Golosiiv, Kiev 022 252650; sergeev@terskol.com

⁸Institute of Theoretical Physics and Astronomy, Vilnius University, Vilnius, Lithuania; jr@itpa.lt

⁹Ulupinar Observatory, Çanakkale Onsekiz Mart University, Turkey

¹⁰Astronomical Observatory of the Jagiellonian University, ul. Orla 171, 30-244 Cracow, Poland; szola@oa.uj.edu.pl

¹¹Mount Suhora Observatory, Cracow Pedagogical University, Ul. Podchorazych 2, 30-084 Krakow, Poland; zola@astro1.as.ap.krakow.pl

¹²Institut für Astrophysik, Universität Wien, Türkenschanzstrasse 17, 1180 Wien, Austria

that include parameterized, complex carbon and oxygen core composition profiles to fit the periods. Recent spectroscopic analyses place GD358 near the red edge of the DBV instability strip, at $24,000 \pm 500$ K and a $\log g$ of 7.8 ± 0.08 dex. The surface gravity translates to a mass range of 0.455 to 0.540 M_{\odot} . Our best fit model is slightly more massive and much hotter (by 2,000 K) than the most recent spectroscopy indicates. We find a pure helium layer mass of $10^{-5.40}$, consistent with a red edge object when compared with other DBVs analyzed using the same models.

Subject headings: Stars: oscillations — Stars: variables: general — white dwarfs

1. Astrophysical Context

White dwarfs are the end product of evolution for around 98% of the stars in our Galaxy. Buried in their interiors are the records of physical processes that take place during earlier stages in the life of the star. Nuclear reaction rates during the core helium burning phase set the core composition of white dwarfs, while the relative time spent burning hydrogen and helium during the asymptotic-giant-branch (AGB) phase and mass-loss episodes determine the thickness of the helium layer (Lawlor & MacDonald 2006; Althaus et al. 2005). Helium atmosphere white dwarfs (DBs) comprise roughly 20% of the population of field white dwarfs, with most of the remaining 80% consisting of their hydrogen atmosphere (DA) cousins. The bifurcation into two spectral classes is thought to occur during post-AGB evolution when, in some cases, a very late thermal pulse burns off the residual hydrogen in the envelope, producing a nearly pure helium atmosphere (Iben et al. 1983). Such objects then return to the white dwarf cooling track as PG 1159 stars, which are widely believed to be the precursors of most DB white dwarfs. DBs are found to pulsate at effective temperatures ranging between 21,000 K and 28,000 K (Beauchamp et al. 1999; Castanheira et al. 2005).

The subject of this paper, GD358 (V777 Her) is the brightest ($m_v = 13.7$) and best studied helium atmosphere white dwarf pulsator. It is located near the red edge of the instability strip, with a spectroscopic temperature of $T_{\text{eff}} = 24000 \pm 500$ K and $\log g = 7.8$ (Koester 2013). GD358’s pulsation spectrum contains a series of independent modes, many with complex frequency structure. Models involving magnetic fields and oblique rotation have been proposed to explain that structure (Montgomery et al. 2010).

Since the 2006 Whole Earth Telescope (WET) run reported in Provencal et al. (2009), we have maintained an active observing program of GD358 in an effort to identify additional frequencies in this complex star. These new observations have identified additional periods

in GD358’s pulsation spectrum, bringing the total known modes to 15. Thirteen of these modes belong to a consecutive $\ell = 1$ sequence, the longest sequence observed in a DBV.

Paradoxically, among the DBVs with enough detected periods to be fitted asteroseismically, GD358 is the only one that has not been analyzed using the complex C/O profiles adapted and parameterized from stellar evolution calculations (e.g. Salaris et al. (1997); Althaus et al. (2005)). The most recent fits of GD358 (Metcalf et al. 2003) were performed using 11 observed modes and simple models where the oxygen abundance drops linearly from its central value to zero. We present here a new detailed asteroseismic analysis of GD358, taking advantage of its long sequence of $\ell = 1$ modes to better constrain the asteroseismic fits and define the limits of high precision white dwarf asteroseismology.

The present analysis also allows us to place GD358 in the context of stellar evolution. According to the models, the precursors of DBs emerge from the born-again phase with envelopes containing a nearly uniform mixture of helium (He), carbon (C), and oxygen (O) out to the photosphere (Dreizler & Heber 1998; Herwig et al. 1999). As the PG 1159 stars cool, the helium diffuses upward and gradually accumulates to form a chemically pure surface layer. Through the DBV instability strip, this process is still ongoing so that instead of a pure helium layer surrounding the carbon and oxygen core, one has a region where the carbon and helium are still mixed. This leads to a double layered structure, with the pure He surface layer overlying the remainder of the uniform He/C/O envelope, all above the degenerate C/O core. A key prediction of the diffusion models is that, for a given stellar mass, the pure He surface layer will steadily grow thicker as the DB star cools. GD358 is the fourth DBV we can use to check this theory. The other three DBVs (Bischoff-Kim et al. (2014); Sullivan et al. (2008); Metcalfe et al. (2003)) have painted a picture qualitatively consistent with the diffusion calculations, with the hotter best fit models having thinner pure helium layers. With GD358, we seek to confirm this trend.

In Section 2, we present our new observations and outline the data reduction process. In Section 3, we establish the framework for frequency identification, and present the list of frequencies used for the asteroseismic investigation. We perform further analysis of the observed frequencies in Section 4, and motivate the ℓ and m identification of the modes. We present the asteroseismic fitting of GD358’s pulsation spectrum in section 5, present the results in section 6 and discuss our results in section 7.

2. New Observations and Data Reduction

GD358 was discovered in 1982 (Winget et al. 1982) and has been the target of the Whole Earth Telescope (WET) in 1990, 1994, 2000, and 2006 (Provencal et al. 2009; Kepler et al. 2003; Winget et al. 1994). New observations presented here include 254 individual observing runs (1105.1 hrs) spanning 2007-2015 (Table 1). Each season of observations was obtained as part of multisite WET campaigns (Nather et al. 1990).

Data reduction follows the steps described in Provencal et al. (2012). In brief, the new observations were obtained with different CCD photometers, each with distinct effective bandpasses. We minimize the bandpass issues by using CCDs with similar detectors whenever possible and employing a red cutoff filter (BG40 or S8612) to normalize wavelength response and reduce extinction effects. We corrected each image for bias and thermal noise, and normalized by the flat field. Aperture photometry using the Maestro photometry pipeline described by Dalessio et al. (2010) was performed on each image, utilizing a range of aperture sizes for the target and comparison stars. For each individual nightly run, we chose the combination of aperture size and comparison star(s) producing the highest signal/noise light curve.

We used the WQED pipeline (Thompson & Mullally 2009) to examine each nightly light curve for photometric quality, remove outlying points, divide by suitable comparison stars, and correct for differential extinction. Our observational technique is therefore not sensitive to oscillations longer than a few hours. The result is a series of light curves with amplitude variations represented as fractional intensity (mmi). The unit is a linear representation of the fractional intensity of modulation ($1 \text{ mmi} \approx 1 \text{ mmag}$). We present our Fourier transforms (FTs) in units of modulation amplitude ($1 \text{ mma} = 1 \times 10^{-3} \text{ ma} = 0.1\% = 1 \text{ ppt}$).

The final reduction step is to combine the individual light curves (an example is shown in Fig. 1) to produce complete light curves for GD358 for each observing season. We assume GD358 oscillates about a mean light level. This assumption allows us to carefully assess overlapping segments from different telescopes and identify and correct any vertical offsets. As discussed in detail in Provencal et al. (2009), we find no significant differences between the noise levels of amplitude spectra using: 1) the combination of all light curves including overlapping segments from different telescopes, 2) the combination of light curves where we retain only higher signal to noise observations in overlapping segments and 3) combining all light curves using data weighted by telescope aperture.

The complexities associated with GD358’s pulsations (see Section 3) led us to also reduce all available archival data (Provencal et al. 2009; Kepler et al. 2003; Winget et al. 1994, 1982) insure continuity in methodology. The final result is a series of light curves for

each observing season between 1982 and 2015. For the new observations, 2007 contains 8.1 hrs of observation, 2008 26.1 hrs, 2009 45 hrs, 2010 201.3 hrs, 2011 401.1 hrs, 2012 150.5 hrs, 2013 87 hrs, 2014 184.6 hrs, and 2015 55 hrs. Our coverage is not complete, and this incompleteness produces spectral leakage in the amplitude spectra. To quantify this, we sampled single sinusoids using exactly the same times as the original data for each season. The resulting amplitude spectrum, or “spectral window”, is the pattern produced in the FT by a single frequency. The FTs for 2010, 2011, and 2014 are given in Fig. 2.

3. Frequency Identification

Our goal is to compile a complete list of GD358’s observed independent and combination frequencies to be used in a comprehensive asteroseismic analysis. GD358 is known for large scale changes in amplitudes and small but not insignificant frequency variations on a variety of timescales (Provencal et al. 2009; Kepler et al. 2003). The amplitude and frequency variations evident in Fig. 2 demonstrate that it is not feasible to analyze the entire data set as one unit. To minimize the effects of the long term amplitude and frequency variations, we analyze the light curves from each observing season individually.

We use *Period04* (Lenz & Breger 2005) for Fourier analysis and nonlinear least squares fitting to select statistically significant peaks in each FT. We adopt the criterion that a peak must have an amplitude at least four times greater than the average noise level in the given frequency range (Provencal et al. 2012). We define “noise” as the frequency-dependent average amplitude after removal of the dominant frequencies. This is a conservative estimate, as it is impossible to ensure that all of the “real” frequencies are removed when determining the noise level. This is certainly true for GD358, where the peaks above $\approx 2500 \mu\text{Hz}$ are combination frequencies (see Section 4.2, Provencal et al. (2009)). Fig. 3 displays the average noise as a function of frequency for the 2007-2015 observing seasons. A similar plot for the archival data is presented in Fig. 3 of Provencal et al. (2009). To confirm our uncertainty estimates, we calculated Monte Carlo simulations using the routine provided in *Period04*. This routine generates a set of light curves using the original times, the fitted frequencies and amplitudes, and added Gaussian noise. A least squares fit is performed on each simulated light curve, with the distribution of fit parameters giving the uncertainties. Our Monte Carlo results are consistent with our average noise estimates.

Having established our baseline noise levels, we proceed to frequency selection and identification. Our frequency selection procedure involves identifying the largest amplitude resolved peak in the FT, fitting a sinusoid at that frequency to the data set, subtracting the fit from the light curve, recomputing the FT, examining the residuals, and repeating the

process until no significant power remains. This technique, known as prewhitening, must be employed with an over-abundance of caution, especially since we are aware of amplitude and/or frequency modulation in our data set. A detailed discussion of the prewhitening procedure and steps taken to minimize the effects of amplitude modulation is given in (Provencal et al. 2009). Our final identifications of independent frequencies detected in each observing season are given in Table 2 and Table 3.

4. Frequency Analysis

4.1. Frequencies Distribution

Perusal of Tables 2 and 3 shows that GD358’s observed frequencies vary in two important ways. First, frequencies detected in a given observing season are not found in all observing seasons. Asteroseismology is based on the assumption that the available pulsation frequencies are linked to stellar structure. Since we are fairly certain that GD358’s internal structure does not change on the timescales of the observations, we can assume that GD358 excites different subsets of its available pulsations at different times. While this is a common phenomenon seen in white dwarf pulsators, the selection mechanism remains unknown. The best way to determine GD358’s complete set of pulsation frequencies is to combine frequency identifications from multiple observing seasons as outlined in Kleinman et al. (1998).

Fig. 4 presents a schematic representation of GD358’s independent frequencies detected between 1982 and 2015. The features of asteroseismic importance are the localized bands between 900 and 2400 μHz (1100 and 400 s). We interpret the bands to represent a series of radial overtone k . The bands themselves illustrate the second way in which GD358’s frequencies vary. Each band consists of frequency detections from multiple observing seasons, but each band is significantly wider in frequency space than the frequency error of any single measurement, arguing that some process is acting on the frequencies. The simplest explanation is rotational splitting. However, with the exception of the two highest frequency (shortest period) bands ($k = 8$ and $k = 9$ from Provencal et al. (2009)), we find no clear evidence of multiplet structure in the frequency distributions of the lower frequency (longer period) bands (Fig. 5). The lower frequency band widths are most likely the result of some process producing amplitude and/or frequency modulation that obscures any underlying signatures of rotational splitting.

Fig. 4 also shows that the widths of the bands are not constant, but change from band to band. Bell et al. (2015) presents an interesting analysis of the hydrogen atmosphere pulsator (DAV) KIC4552982, in which they identify 17 bands of pulsation frequencies. KIC4552982

is one of the coolest ZZ Ceti known (Tremblay et al. 2013), and it follows the general pattern exhibited by GD358: the highest frequency (shortest period) mode shows evidence of rotational splitting, while the lower frequency (longer period) modes are complex bands. The authors note that this DAV’s bands have different widths in frequency space, and that there may be astronomical significance to this. Although the observational timebases and coverage are quite different (20 continuous months for KIC4552982 vs 33 incomplete years for GD358), our data presents the opportunity to investigate this for a cooler DB pulsator. We measured the widths of each of GD358’s band where we have more than 10 detections. We define “width” as the difference between the lowest and highest frequency detected in each band. Fig. 6 presents the results. We find no correlation of width with number of detected peaks in each band. Interestingly, the widths of GD358’s bands are commensurate with those found in KIC4552982. We find a general increase in width with decreasing frequency (increasing period), until we reach the band at 1238 μHz (807 s). This band has a width at least twice as wide as any other.

A second interesting behavior is given by the distribution of average amplitudes for the bands (Fig 4). In particular, the two bands at 1857.7 and 2007.6 μHz have never been observed at amplitudes above 4 mma. The band at 1369 μHz is also only observed at lower amplitudes. Interestingly, the band at 1741.5 μHz was not observed at large amplitude prior to 2006, and it has remained at high amplitude since that time.

In broad brush strokes, the observed global pulsations involve the whole star, but each pulsation samples the star in slightly different ways. For example, modes with lower frequencies (higher radial k values) preferentially sample the outer layers, while modes with higher frequencies (lower radial k values) have outer turning points that are farther from the surface, and so sample the deeper interior. It makes intuitive sense that lower frequency modes would be affected by processes confined to the outer stellar atmosphere. We speculate that the observed band widths and pulsation amplitudes contain information about the convection zone and/or any surface magnetic field. Further investigation requires guidance from theory.

4.2. Mode Identification

Our current work has produced a well defined sequence of modes, adding to previous studies (Montgomery et al. 2010; Provencal et al. 2009; Metcalfe et al. 2000; Winget et al. 1994). The previous identification of these modes as a series of $l=1$ radial overtones is based mostly on the pulsation frequency distribution and limited spectroscopic analysis (Kotak et al. 2002; Castanheira et al. 2005). It is important to further investigate these

identifications as we initiate an indepth asteroseismic investigation.

GD358’s combination frequencies provide a tool by which we can bolster ℓ identifications. Combination frequencies are typically observed in the FTs of moderate to large amplitude pulsators. They are identified by their exact numerical relationships with parent frequencies. The combinations themselves are not independent, but result from nonlinear effects associated with the surface convection zone (Brickhill 1992; Brassard et al. 1995; Wu 2001; Ising & Koester 2001). Wu (2001) lays the groundwork, showing that observed amplitudes of the combination frequencies depend on geometric factors such as the (ℓ, m) indices of the parents and the inclination of the pulsation axis to the line of sight.

The methods outlined in Provencal et al. (2012) and Montgomery et al. (2010) work best when applied to larger amplitude frequencies detected in high signal to noise data sets such as provided by extensive WET runs. The primary reason for this is that combination frequencies are lower amplitude than their parents, and so are more difficult to detect in sparse data. We chose the 1990, 1994, 2006, 2010, 2011, and 2014 observing seasons, and looked at pulsation frequencies with amplitudes above 10 mma.

As an example, Fig. 7 shows the probability distribution of ℓ and m values for the 1735.96 μHz frequency as detected in 2014. To produce the distribution, we ran the amplitude code (Montgomery et al. 2010) 1000 times, and selected the results having $Res_{rms} < 9.5 \times 10^{-06}$, where Res_{rms} are the root-mean-squared residuals between predicted and observed amplitudes. For our example, this mode is clearly preferred as an $\ell = 1, m = 1$ mode. We find similar results for all modes above 10 mma in the 1990, 1994, 2006, 2010, and 2014 observing seasons. Combining the results from the combination frequencies with previous evidence, we are confident that the bands in Fig. 4 represent a series of $\ell = 1$ modes.

Finally, given the $l=1$ identification and the lack of definite multiplet structure for the higher frequency modes, the best way to determine the central frequency for each band is simply to average the detected frequencies in the bands. We experimented with numerous weighting techniques, and determined there is no significant difference in our solutions. Our final frequencies for each band are given in Table 4. We use these periods in our asteroseismic fitting.

5. Asteroseismic fitting

The basic method in our asteroseismic fitting consists of calculating grids of white dwarf models and running a fitting subroutine to match the periods of the models (P^{obscale}) with the observed periods P^{obs} . Following standard statistical methods, each fit is assigned a

fitness parameter calculated the following way:

$$\sigma_{\text{RMS}} = \sqrt{\frac{1}{W} \sum_1^{n_{\text{obs}}} w_i (P_i^{\text{calc}} - P_i^{\text{obs}})^2}, \quad (1)$$

$$W = \frac{n_{\text{obs}} - 1}{n_{\text{obs}}} \sum_1^{n_{\text{obs}}} w_i \quad (2)$$

where n_{obs} is the number of periods present in the pulsation spectrum and the weights w_i are the inverse square of the uncertainties listed for each period in table 4. We note that the two shortest period modes have 6000 times the weight of the longest period mode. Another way to think about this is to assume we have a calculated period that matches the highest period mode very poorly, being 20 seconds away. 20 seconds is roughly half the average period spacing for $\ell = 1$ modes in the relevant area of parameter space and so it is the worse period fit one can get. In order to have the same impact on σ_{RMS} , the lowest period mode would have to match to within 0.26 seconds. In essence this is almost ignoring the modes that have a period measurement uncertainty of 0.5 s or more. It is, however completely consistent with the relative uncertainty on the periods.

5.1. The Models

To compute our models, we used the White Dwarf Evolution Code (WDEC). The WDEC evolves hot polytrope models from temperatures above 100,000 K down to the temperature of our choice. Models in the temperature range of interest for the present study are thermally relaxed solutions to the stellar structure equations. Each model we compute for our grids is the result of such an evolutionary sequence. The WDEC is described in detail in Lamb & van Horn (1975) and Wood (1990). We used smoother core composition profiles and implemented more complex profiles that result from stellar evolution calculations (Salaris et al. 1997). We updated the envelope equation of state tables from those calculated by Fontaine et al. (1977) to those given by Saumon et al. (1995). We use OPAL opacities (Iglesias & Rogers 1996) and plasmon neutrino rates published by Itoh et al. (1996).

DBVs are younger than their cooler cousins the DAVs. Time-dependent diffusion calculations (e.g. Dehner & Kawaler 1995; Althaus et al. 2005) show that at 24,000 K, a typical temperature for a DBV, the carbon has not yet fully settled into the core of the star. We expect the helium layer to be separated into a mixed He/C layer with a pure He layer on

top, as shown in Fig. 8. Following Metcalfe et al. (2005), we adopted and parameterized this structure in our models.

5.2. Initial Grid Search

In our asteroseismic fits, we initially varied six parameters; the effective temperature, the mass and four structure parameters. There are two parameters associated with the shapes of the oxygen (and carbon) core composition profiles: the central oxygen abundance (X_o) and the edge of the homogeneous carbon and oxygen core (q_{fm} , as a fraction of stellar mass). For envelope structure, M_{env} marks the location of the base of the helium layer and M_{He} the location where the helium abundance rises to 1 (see Fig. 8). M_{env} and M_{He} are mass coordinates, defined as e.g. $M_{\text{env}} = -\log(1 - M(r)/M_*)$, where $M(r)$ is the mass enclosed in radius r and M_* is the stellar mass.

We started with a master grid (Table 5) chosen so that it covered all relevant area of parameter space and had sufficient resolution to find any region of local minimum in the fitness parameter (Bischoff-Kim & Metcalfe 2011; Bischoff-Kim et al. 2014). We used the minimum resolution that was computationally manageable. The master grid involved the computation of 10,483,200 models. We fit simultaneously all 15 periods, requiring all of them to be $\ell = 1$ modes. A fitness map of this initial fit are shown in the left panel of Fig. 9, and the parameters of the best fit model are listed in Table 5.

5.3. Asymptotic Period Spacing

Before we refine the period-by-period fitting optimization, it is worthwhile to step back and consider what we can learn from the average period spacing of GD358. The average period spacing provides an asteroseismic measure of the mass and temperature of the star, independent of the details of internal chemical composition profiles. Higher k modes are not strongly trapped in the core and according to asymptotic theory, they should be nearly evenly spaced in period. This spacing is given by (Unno et al. 1989)

$$\Delta P = \frac{\pi}{\ell(\ell + 1)^{1/2}} \left[\int_{r_1}^{r_2} \frac{N}{r} dr \right]^{-1}, \quad (3)$$

where r_1 and r_2 are turning points of the mode and N is the Brunt-Väisälä frequency. The asymptotic period spacing is ℓ dependent, with higher ℓ modes having smaller spacing. In the case of GD 358, we have a single $\ell = 1$ sequence so we only need to worry about the

dependence of the asymptotic period spacing on the Brunt-Väisälä frequency. Much if not all of GD 358’s pulsation spectrum is close to the asymptotic limit, because the shortest period observed is a $k = 8$ mode.

The dependence of ΔP on the Brunt-Väisälä frequency leads to higher mass and lower temperature models having a smaller period spacing (their interior is less compressible). This effect appears in asteroseismic fitting of white dwarfs and also sdB stars as a ubiquitous diagonal trend in contour maps of the quality of the fits in the mass-effective temperature plane (e.g Bischoff-Kim et al. 2014; Castanheira & Kepler 2009; Charpinet et al. 2008). One requirement for the periods of the model to match the observed periods is that the average period spacing in the models matches the average period spacing in the observed pulsation spectrum. If a good match occurs for a given mass and effective temperature, then models with lower mass but higher effective temperature will also match well.

We use the sequence of 13 consecutive $\ell = 1$ modes found in GD358’s pulsation spectrum to calibrate our models. Using the $\ell = 1$ sequence of modes, we compute an average period spacing of 39.08 seconds. We call this ΔP_{obs} . For each model in the master grid, we compute an asymptotic period spacing (ΔP_{calc}). This asymptotic period spacing is calculated by first discarding the 10 lowest k modes. The exact value of 10 is somewhat arbitrary, but it is chosen so that the modes we use in our computation are indeed in the asymptotic limit. The higher k modes show weaker trapping than the lower k modes. We then fit a line through the set (k_i, P_i) . The slope gives us the asymptotic period spacing in the model. We also calculate the residuals of the fits and discard the models that have residuals above a certain limit. The limit is chosen by checking the procedure by eye on a few models.

We show a contour map of the location of the models that best match the average period spacing of 39.08 seconds in Fig. 9, right panel. We place it side by side with a contour map showing the location of the best fit model in the same region of parameter space, based on the master grid fitting described in section 5.2. Note how the best fit model falls right within the valley where the period spacings between GD358 and the models match. This should come as no surprise, as in order for 15 periods to fit reasonably well, the model period list should have a spacing similar to that of the observed period spectrum. The most recent spectroscopic determination of Koester (2013) is far off the valley, at 24,000 K and $0.506^{+0.034}_{-0.051} M_{\odot}$. Previous spectroscopic determinations, such as that of Bergeron et al. (2011), do fall within the swath where the period spacings match. We show the spectroscopic data point of Bergeron et al. (2011) in Fig. 9. The best fit model from the period by period fit lies further down the valley.

One can fit simultaneously the average period spacing and the individual periods formally while performing the fits by using some prescription to calculate the goodness of fit.

This leads to a more complex relation than defined in equation 1. Note that the period spacing is a much weaker constraint than the individual period fit. If one takes 5.0 seconds as an upper limit for goodness of fit, that includes 9 points in the period-by-period fit plot (left panel in Fig 9), but the entire parameter plane for the average period spacing fit plot (right panel). We bypass the difficulty of assigning proper weights to each constraint by taking the average period spacing fit into account as an initial step to refine our fits. We refine our fits by calculating models on a higher resolution grid that fall within the region defined by the two diagonal lines shown in the right panel of Fig. 9 (covering the effective temperature range 25,000 K-27,500 K), then performing a period-by-period fit using equation 1.

5.4. Optimal Grid Resolution

Having determined a more restricted region of parameter space to search for the best fit models, we now turn to the question of how fine we need to make our refined grid. We want to have a high enough resolution grid that we can be sure we captured a true minimum, but on the other hand, there are computational limitations to how many models we can afford to calculate, save, and process.

One way to gain a sense of how fine the grid needs to be is to make single parameter cuts through parameter space. Fig. 10 shows such cuts for master grid models. The plot was made by fixing 5 of the 6 parameters to the best fit values of the best initial fit (see table 5). For some parameters, the fits seem to settle to a minimum in a smooth way, while for others, they exhibit jumps. For instance, the spike in the effective temperature plot at 27,800 K is due to a period (around 530 s) that goes away and then comes back. The model with the missing period fits poorly compared to the models on either side of it. The jump from $\sigma_{\text{RMS}} \sim 5$ to $\sigma_{\text{RMS}} \sim 30$ that happens from 28,400 K to 28,600 K is due to a discontinuous change in the period spectrum of the models. Namely, the appearance of a new mode between the 710 and 784 s modes of the 28,400 K model.

Discontinuities like these are unsettling, as it is easy to see that one might miss a best fit model if the grid is not fine enough. In order to quantify "fine enough", we ran systematic scans, computing models with 5 parameter fixed and allowing the 6th parameter to vary in very fine steps. We went down in step sizes to $\Delta T_{\text{eff}} = 1$ K, $\Delta M_* = 0.0001 M_{\odot}$, $\Delta M_{\text{env}} = \Delta M_{\text{He}} = 0.01$ dex, $\Delta X_o = 0.01$, and $\Delta q_{\text{fm}} = 0.001$. Regardless of the behavior of individual modes in the models as the parameters vary, we can assert what step sizes will allow us to minimize our risk of missing a minimum. We settled on step sizes of $\Delta T_{\text{eff}} = 50$, $\Delta M_* = 0.0001$, $\Delta M_{\text{env}} = 0.1$, $\Delta M_{\text{He}} = 0.1$, $\Delta X_o = 0.1$, and $\Delta q_{\text{fm}} = 0.005$ for our refined grid.

6. Results of the Period Fitting

The parameters for our best fit model based on the refined grid are listed in Table 5 and the periods of that model in Table 4. The goodness of fit of the model is $\sigma_{\text{RMS}} = 0.964$ s. We also list the Bayes Information Criterion (BIC) number, a statistic that normalizes the quality of fits by number of free parameters and number of constraints for comparison with other studies. For a discussion applied to this parameter study, see Bischoff-Kim & Metcalfe (2011). A negative BIC indicates a good quality of fit, given the number of constraints. One should keep in mind that the quality of fit is aided by the fact that some of the periods have large uncertainties.

In Fig. 11 we focus on the mass dependence of the fitness parameter to illustrate the effect a finer grid has on the fitting. We could have used less of a fine mesh in mass, but with our very fine mesh, we do get a better view of how the discontinuities first shown in Fig. 10 behave and that they are not true discontinuities, just large changes in goodness of fit for small changes in mass.

Finally, we show the interior structure of the best fit model in Fig. 8, with the corresponding Brunt-Väisälä frequency profile.

6.1. Validation of the Fitting Method

With what we have discovered in section 5.4, it is only natural to be concerned about whether we have truly found a best fit. We performed a simple test to validate our fitting method, which consisted of using the exact same procedure to find a best fit to the periods of a model that was not on any of the grids we calculated, but that did have parameters that were very close to the best fit model. We used the period list for a model with parameters $T_{\text{eff}} = 25570$ K, $M_*/M_{\odot} = 0.5437$, $M_{\text{He}} = -5.30$, $X_o = 0.42$, and $q_{\text{fm}} = 0.175$, fixing M_{env} to -2.80, and including only the subset of 15 $\ell = 1$ periods that match GD358’s pulsation spectrum.

We first performed a fitting of the periods using the master (coarse) grid described in section 5.2. This placed the best fit model in the appropriate region of parameter space. Then we refined our fits, using the grids described at the end of section 5.3. We are able to recover the best fit parameters adequately, with the top 10 best fit models having parameters $T_{\text{eff}} = 25620 \pm 67$ K, $M_*/M_{\odot} = 0.5431 \pm 0.0011$, $M_{\text{He}} = -5.32 \pm 0.098$, $X_o = 0.40$ for all top 10 fits, and $q_{\text{fm}} = 0.175 \pm 0.5$. The top 10 best fits have $\sigma_{\text{RMS}} \sim 0.5$ s. We remind the reader that the step sizes in the second phase of the fitting are 20 K for T_{eff} , 0.2 for M_{He} , 0.2 for X_o , and 0.01 for q_{fm} .

7. Discussion and Conclusions

We analyzed archival data and over a thousand hours of new observations on GD358, together covering a span of 33 years. This allowed us to extract 15 frequencies. This adds 4 modes to the 11 modes known previously. We performed a new asteroseismic fit of GD358 with the new modes and with models that include carbon and oxygen core composition profiles based on the stellar evolution models of Salaris et al. (1997).

We find a best fit effective temperature of 25,560 K for GD358, hotter than the recent spectroscopic determination of 24000 K (Koester 2013) by 2,000 K (4 sigmas). Our best fit model has a mass of $0.5438 M_{\odot}$, a little over one sigma above the spectroscopic mass. For reasons discussed in section 5.3, while it is possible to determine whether a star is closer to the red edge or the blue edge of the instability strip, effective temperature is poorly constrained in asteroseismic fitting. As we can see from Fig. 10, there are local minima that are almost as good as the global minimum we found, some at lower effective temperature. *However*, the fact that the spectroscopic data point of Koester (2013) falls far off the asymptotic period spacing trend (Fig. 9, right panel) is a concern. This is a profound inconsistency that needs to be resolved.

In fitting GD358, we discovered that the best fit parameter space was semi-chaotic, with two very close sets of parameters able to yield very different fitness number. This is due to the fact that some periods can change values drastically for a small change in a given parameter. The phenomenon is only semi-chaotic, as the period will oscillate between two values. This is good news, because there remains a well defined minimum in parameter space, even if it is a double valued minimum. Any search algorithm that uses a small enough mesh should be able to find the minimum. This phenomenon likely became apparent while fitting GD358 because it is the first white dwarf for which we fit a long consecutive sequence of modes of the same ℓ with high resolution grids.

In this study, we varied the parameters that have traditionally been varied in this type of asteroseismic fitting, so that we can place our results side by side with other studies of DBVs, including KIC 8626021 (Bischoff-Kim et al. 2014), EC200058 (Bischoff-Kim & Metcalfe 2011), and CBS114 (Metcalfe et al. 2005). We now have 4 DBVs that were the object of asteroseismic fitting that used a consistent set of models. Unfortunately, GD358 does not fit neatly into the trend (neither does EC20058). It is true, however that the two blue edge objects (EC20058 and KIC 8626021) have thinner helium layers ($M_{\text{He}} = -6.10$ and -7.90 respectively) than the red edge stars ($M_{\text{He}} = -5.40$ for GD358 and -5.94 for CBS114). Pinning down the proper effective temperature of each star is challenging. To be fully consistent, it is best to use the asteroseismic values, even if effective temperature is not strongly constrained asteroseismically. At best we can contrast blue edge versus red edge

objects.

Numerical experiments of the type presented in section 5.4 have shown that, consistent with the theory of non-radial oscillations, the shapes of the transition zones matter as much as where the transition zones occur (Bischoff-Kim 2015). Modern asteroseismic fitting vary parameters attached to the shape of transition zones (Giammichele et al. 2015). We refrained from doing this in the present study because we wanted to compare our results with previous studies of DBVs. It is unclear how much of an effect on structure parameters a change in parameterization would have.

With data spanning a long period of time, we learn about the stability of the different modes. We find that the shorter period modes tend to be more stable, while the longer period modes tend to vary more in frequency over time. *ellBELL* et al. (2015) have observed and modeled such stochastic behavior in KIC 4552982, a red edge DAV observed nearly continuously for 1.5 years by *Kepler*. In that star, the 361.58 s triplet has sharply defined peaks, while the rest of the modes, with much higher overtone numbers, are less stable. The stability of the low k modes is likely due to the fact that they are strongly trapped in the core. Unlike their higher k counterparts, they are affected very little by the convection zone near the surface.

Facilities: MCAO:0.6m (), Struve(), KPNO:2.1m (), , BOAO:1.8m (), Lulin:1.8m (), Beijing:2.16m (), Maidanek:1.5m (), Peak Terskol

REFERENCES

- Althaus, L. G., Serenelli, A. M., Panei, J. A., Córscico, A. H., García-Berro, E., & Scóccola, C. G. 2005, *A&A*, 435, 631
- Beauchamp, A., Wesemael, F., Bergeron, P., Fontaine, G., Saffer, R. A., Liebert, J., & Brassard, P. 1999, *ApJ*, 516, 887
- Bell, K. J., Hermes, J. J., Bischoff-Kim, A., Moorhead, S., Montgomery, M. H., Østensen, R., Castanheira, B. G., & Winget, D. E. 2015, *ApJ*, 809, 14
- Bergeron, P., et al. 2011, *ApJ*, 737, 28
- Bischoff-Kim, A. 2015, in *Astronomical Society of the Pacific Conference Series*, Vol. 493, 19th European Workshop on White Dwarfs, ed. P. Dufour, P. Bergeron, & G. Fontaine, 175

- Bischoff-Kim, A., & Metcalfe, T. S. 2011, MNRAS, 414, 404
- Bischoff-Kim, A., Østensen, R. H., Hermes, J. J., & Provencal, J. L. 2014, ApJ, 794, 39
- Brassard, P., Fontaine, G., & Wesemael, F. 1995, ApJS, 96, 545
- Brickhill, A. J. 1992, MNRAS, 259, 529
- Castanheira, B. G., & Kepler, S. O. 2009, MNRAS, 396, 1709
- Castanheira, B. G., Nitta, A., Kepler, S. O., Winget, D. E., & Koester, D. 2005, A&A, 432, 175
- Charpinet, S., Van Grootel, V., Reese, D., Fontaine, G., Green, E. M., Brassard, P., & Chayer, P. 2008, A&A, 489, 377
- Dallessio, J., Provencal, J. L., Sullivan, D., & Shipman, H. L. 2010, in 17th European Workshop on White Dwarfs, ed. K. Werner & T. Rauch, AIP Conference Proceedings
- Dehner, B. T., & Kawaler, S. D. 1995, ApJ, 445, L141
- Dreizler, S., & Heber, U. 1998, A&A, 334, 618
- Fontaine, G., Graboske, H. C., J., & Van Horn, H. M. 1977, ApJS, 35, 293
- Giammichele, n., Charpinet, S., Fontaine, G., Brassard, P., & Zong, W. 2015, IAU General Assembly, 22, 2256942
- Herwig, F., Blöcker, T., Langer, N., & Driebe, T. 1999, A&A, 349, L5
- Iben, Jr., I., Kaler, J. B., Truran, J. W., & Renzini, A. 1983, ApJ, 264, 605
- Iglesias, C. A., & Rogers, F. J. 1996, ApJ, 464, 943
- Ising, J., & Koester, D. 2001, A&A, 374, 116
- Itoh, N., Nishikawa, A., & Kohyama, Y. 1996, ApJ, 470, 1015
- Kepler, S. O., et al. 2003, A&A, 401, 639
- Kleinman, S. J., et al. 1998, ApJ, 495, 424
- Koester, D. 2013, private communication
- Kotak, R., van Kerkwijk, M. H., & Clemens, J. C. 2002, A&A, 388, 219

- Lamb, D. Q., & van Horn, H. M. 1975, *ApJ*, 200, 306
- Lawlor, T. M., & MacDonald, J. 2006, *MNRAS*, 371, 263
- Lenz, P., & Breger, M. 2005, *Communications in Asteroseismology*, 146, 53
- Metcalfe, T. S., Montgomery, M. H., & Kanaan, A. 2003, *American Astronomical Society Meeting*, 203
- Metcalfe, T. S., Montgomery, M. H., & Kanaan, A. 2005, in *Astronomical Society of the Pacific Conference Series*, Vol. 334, 14th European Workshop on White Dwarfs, ed. D. Koester & S. Moehler, 465
- Metcalfe, T. S., Nather, R. E., & Winget, D. E. 2000, *ApJ*, 545, 974
- Montgomery, M. H., Provencal, J. L., Kanaan, A., Thompson, S., Dalessio, J., Shipman, H., & Winget, D. E. 2010, *ApJ*, 716, 84
- Nather, R. E., Winget, D. E., Clemens, J. C., Hansen, C. J., & Hine, B. P. 1990, *ApJ*, 361, 309
- Provencal, J. L., et al. 2009, *ApJ*, 693, 564
- . 2012, *ApJ*, 751, 91
- Salaris, M., Dominguez, I., Garcia-Berro, E., Hernanz, M., Isern, J., & Mochkovitch, R. 1997, *ApJ*, 486, 413
- Saumon, D., Chabrier, G., & van Horn, H. M. 1995, *ApJS*, 99, 713
- Sullivan, D. J., et al. 2008, *MNRAS*, 387, 137
- Thompson, S. E., & Mullally, F. 2009, *Journal of Physics Conference Series*, 172, 012081
- Tremblay, P.-E., Ludwig, H.-G., Steffen, M., & Freytag, B. 2013, *A&A*, 559, A104
- Winget, D. E., van Horn, H. M., Tassoul, M., Fontaine, G., Hansen, C. J., & Carroll, B. W. 1982, *ApJ*, 252, L65
- Winget, D. E., et al. 1994, *ApJ*, 430, 839
- Wood, M. A. 1990, PhD thesis, The University of Texas at Austin
- Wu, Y. 2001, *MNRAS*, 323, 248

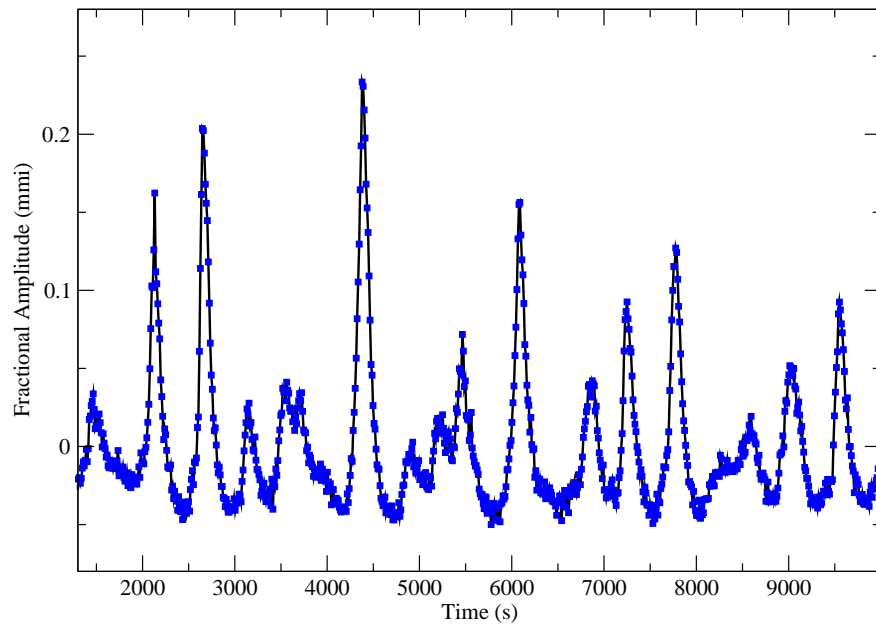


Fig. 1.— Light curve of GD358 obtained with the Peak Terskol 2.0 m telescope. Each point corresponds to a 10 s exposure. The nonlinear, multiperiodic nature of this star is clearly evident. (A color version of this figure is available in the online journal.)

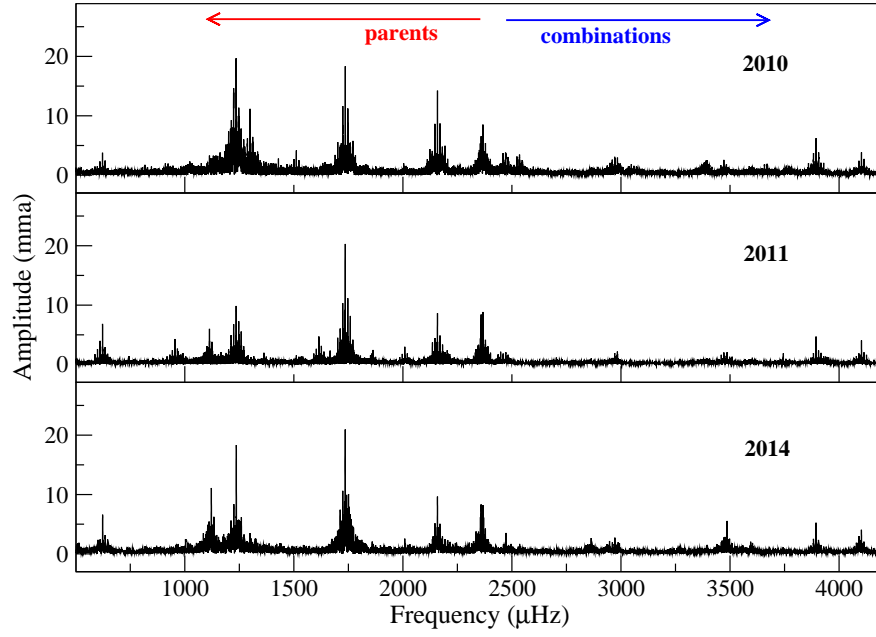


Fig. 2.— Fourier Transforms of GD358 for the 2010, 2011, and 2014 observing seasons. The frequency range of the observed series of $\ell = 1$ modes discussed in Section 4 is indicated by the left arrow (red). Peaks below $\approx 2400 \mu\text{Hz}$ are combination frequencies discussed in Section 4.2 (right arrow, blue). (A color version of this figure is available in the online journal.)

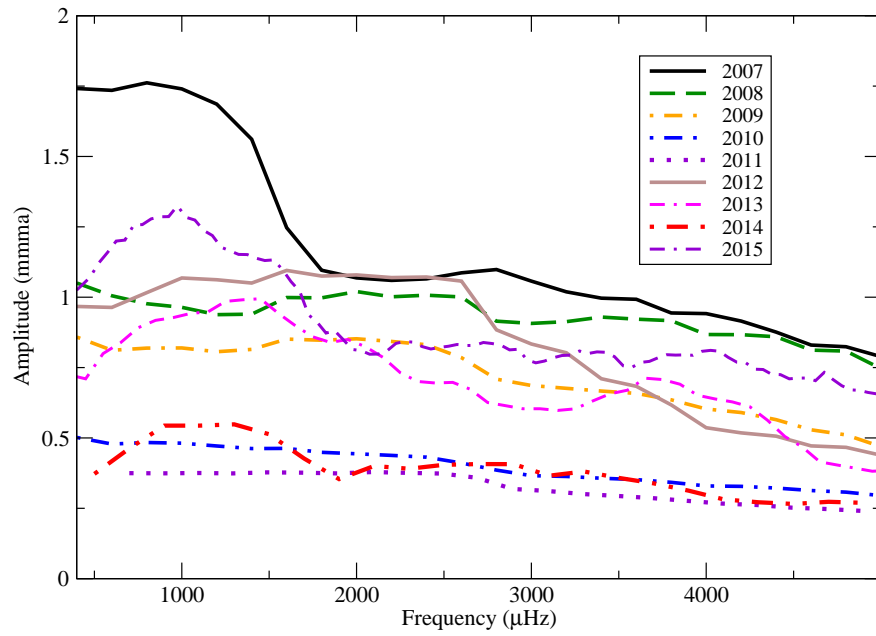


Fig. 3.— A comparison of the average noise as a function of frequency for the 2007-2015 observing seasons. Each data set was prewhitened by its dominant frequencies. The noise levels for each season are somewhat different. This must be taken into account during frequency analysis.

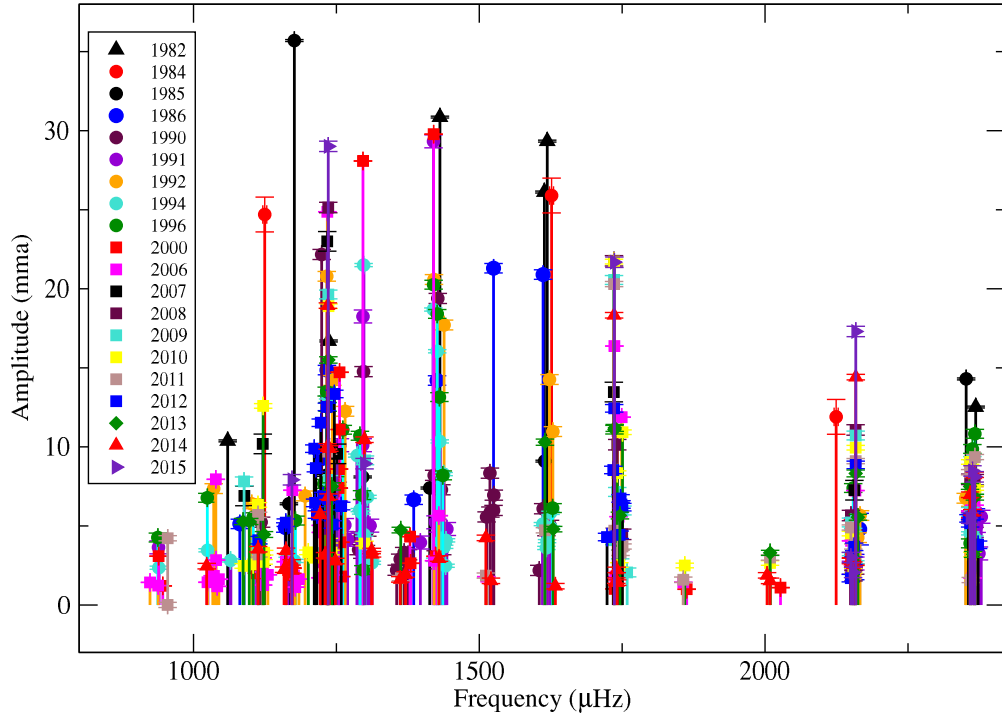


Fig. 4.— A schematic representation of GD358’s pulsation modes for all available data between 1982 and 2015. Systematic patterns of distribution are evident. The bands between 2400 and 1000 μHz (400 and 1000 s) are of particular importance for this work. (A color version of this figure is available in the online journal.)

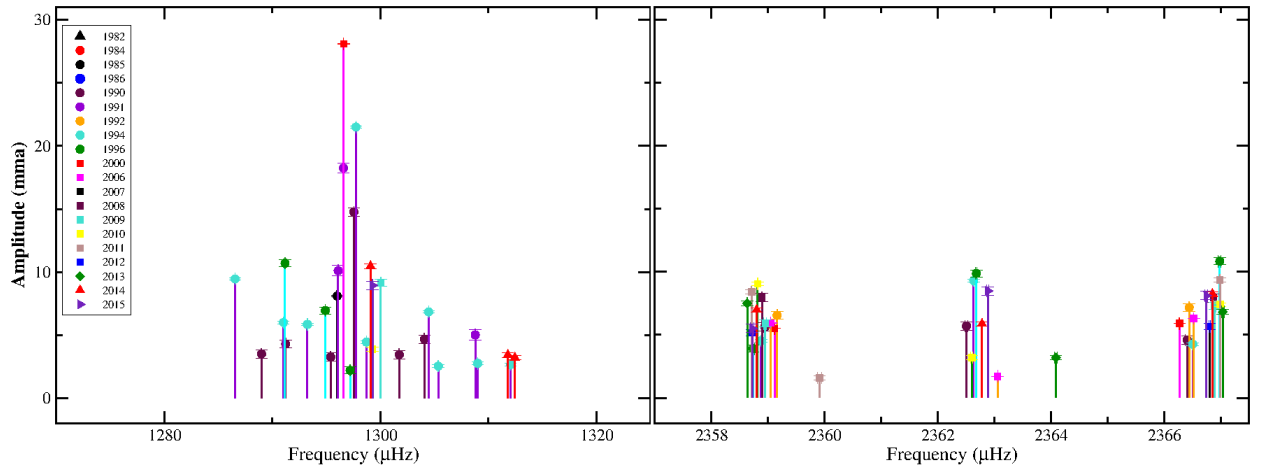


Fig. 5.— The detailed schematic distribution of frequencies for the bands near 1300(*right* and 2360 μHz (*left*). As an example of the higher frequency bands, the 1300 μHz band shows no multiplet structure, unlike the 2360 μHz band. Here we see clear evidence of multiplet structure. Assuming the triplet represents $\ell = 1$, this implies a rotation period of ≈ 1.5 days. Note changes in the x scale for both axes. (A color version of this figure is available in the online journal.)

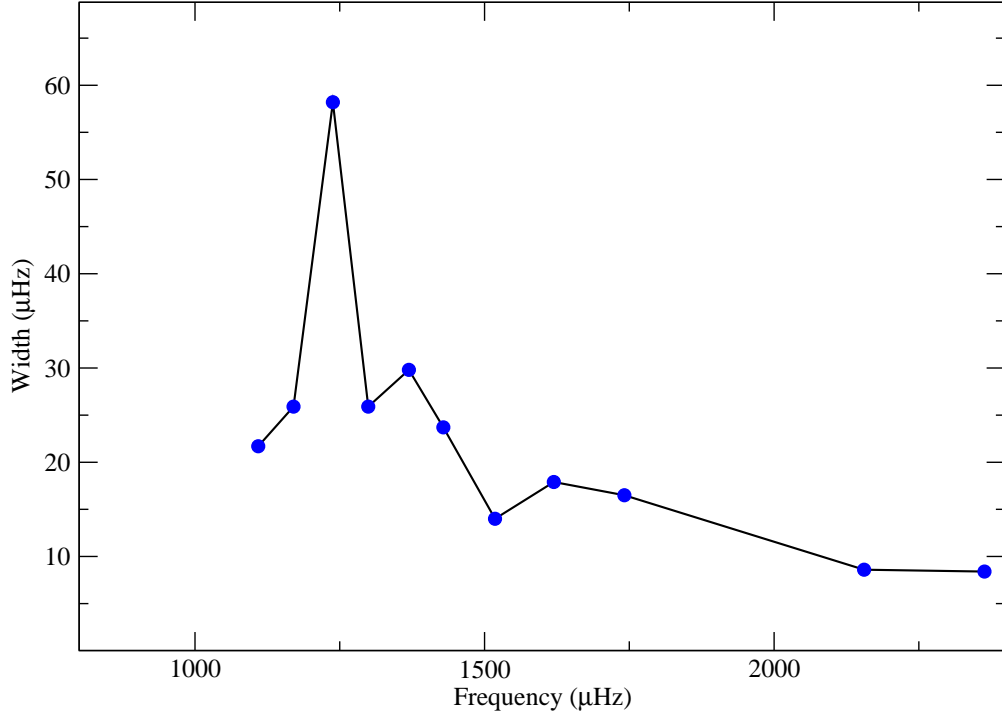


Fig. 6.— Width of each bank of power in Fig. 4. We find an overall increase in band thickness with decreasing frequency (increasing period). The band at 807 s has a width at least twice as large as other bands.

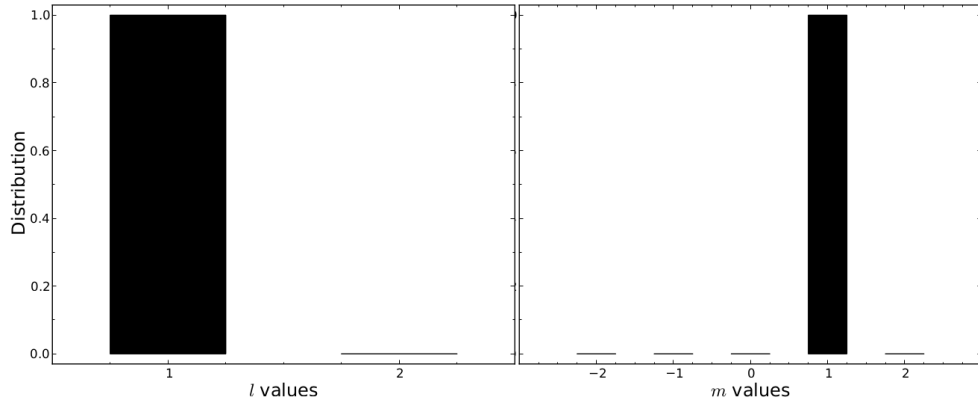


Fig. 7.— Probability distribution (from 0 to 1) of ℓ and m values for the 1735.96 variation detected in 2014. The distribution is produced from 1000 simulations, selecting with $Res_{rms} < 9.5^{-06}$. The amplitudes of the observed combination frequencies argue that this is $\ell = 1$, $m=1$.

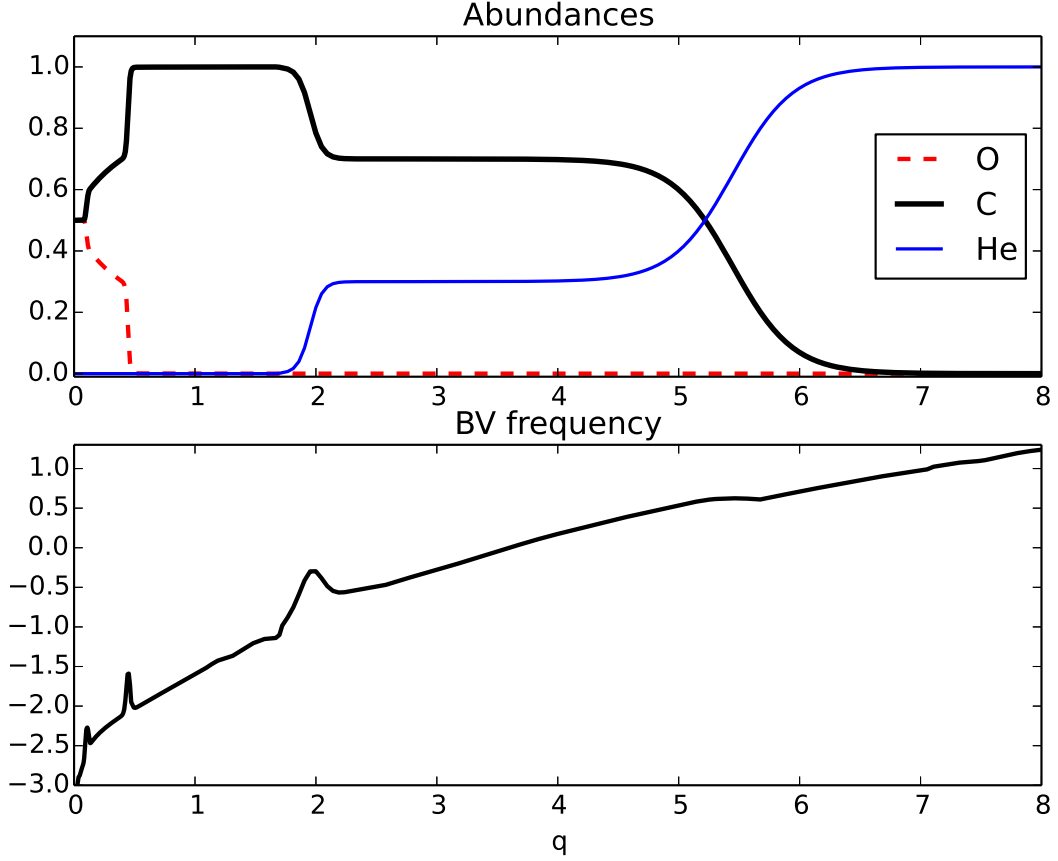


Fig. 8.— *Upper panel:* Chemical composition profiles of the best fit model. The center of the model is to the left and the surface to the right. $q = 2$ corresponds to $M_r = 0.99 M_*$. The vertical axis shows fractional abundances. *Lower panel:* The corresponding Brunt-Väisälä frequency ($\log N^2$ on the vertical axis).

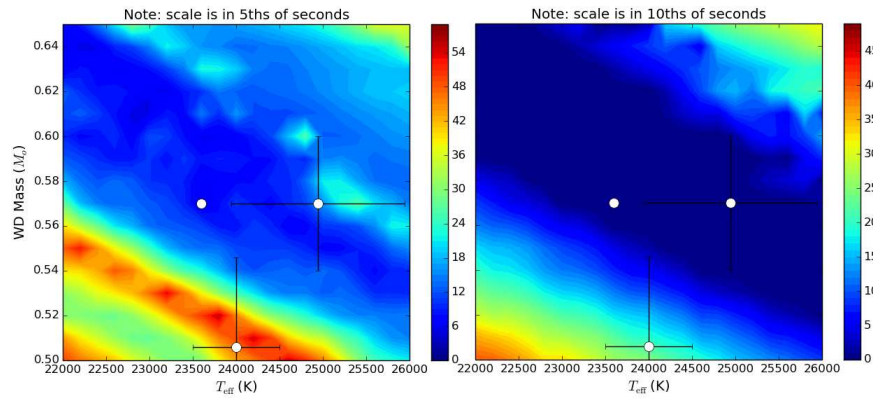


Fig. 9.— *Left panel:* Contour map showing the location of the best fit models. The quantity plotted in the mass-effective temperature plane is the fitness parameter defined in equation 1. *Right panel:* Contour map of the difference between the average periods spacing determined from GD 358’s periods and the asymptotic period spacing of the models, in the mass-effective temperature plane. The scale is in 10s of seconds, so the worse matches pictured on the plot have $|\Delta P_{\text{obs}} - \Delta P_{\text{calc}}| \sim 5$ s. We plotted the spectroscopic mass and temperature determinations of Bergeron et al. (2011) (higher mass), and that of Koester (2013) (lower mass). The point without error bars corresponds to the best initial fit model.

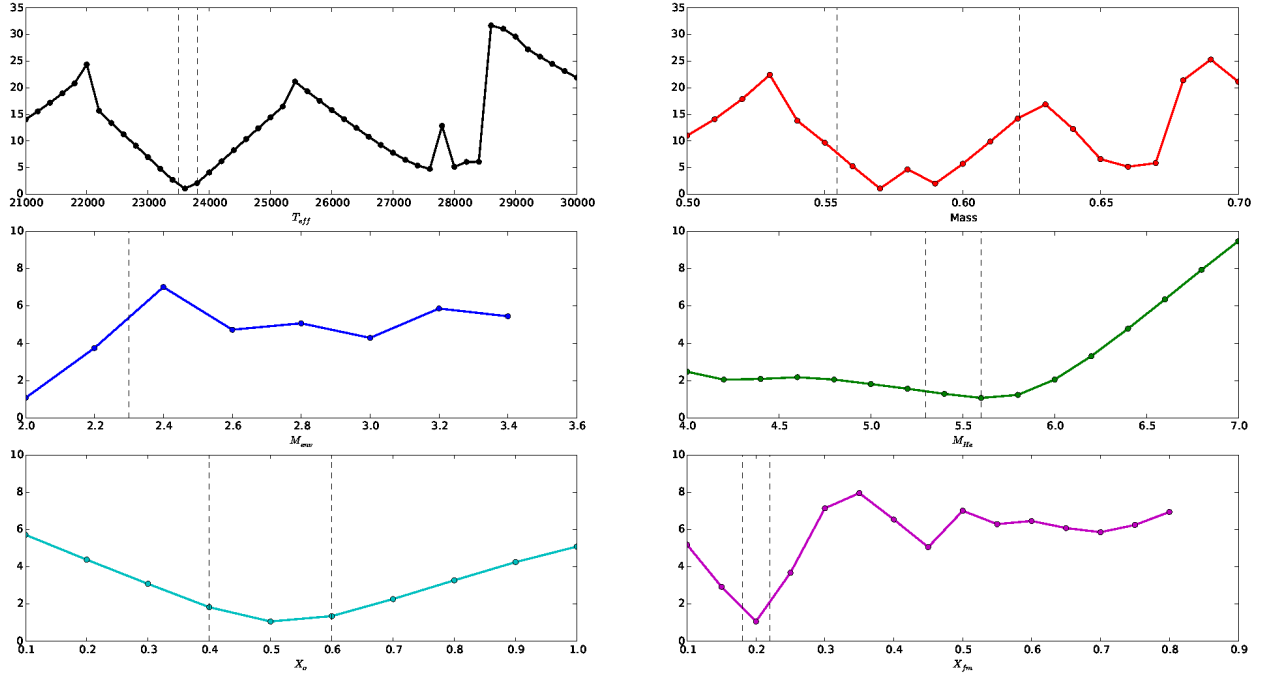


Fig. 10.— Dependence of the fitness parameter on different parameters. The 5 parameters other than the one shown on the horizontal axis in each plot are held to fixed values corresponding to the initial best fit model (table 8). The vertical dashed lines mark the ranges considered in the refined fitting. For the envelope mass, we went up to $M_{env}=2.3$.

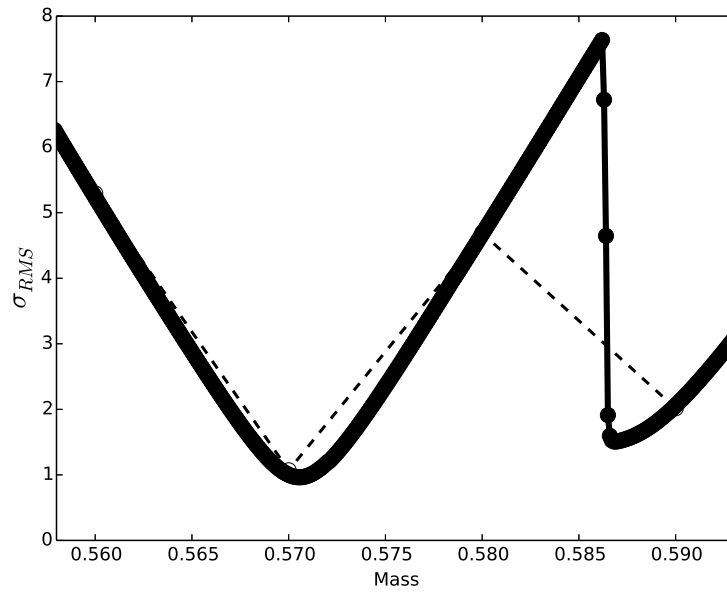


Fig. 11.— Dependence of the fitness parameter on mass alone based on the master grid of models (dashed line) and the refined mesh (solid line).

Table 1.

Run Name	Telescope	Detector	Date	Length (hrs)
mcao070524-01	MCAO 0.6	CCD	2007-05-24	4.0
mcao070531-02	MCAO 0.6	CCD	2007-05-31	4.1
mcao080613-01	MCAO 0.6	CCD	2008-06-13	2.0
mcao080617-02	MCAO 0.6	CCD	2008-07-25	1.2
mcao080726-01	MCAO 0.6	CCD	2008-07-26	1.7
mcao080730-01	MCAO 0.6	CCD	2008-07-30	3.5
mcao080802-01	MCAO 0.6	CCD	2008-08-02	3.7
pjmo080706-03	PJMO 0.6	CCD	2008-07-06	5.1
suho080810-19	Suhora 0.6	CCD	2008-08-10	4.7
suho080811-19	Suhora 0.6	CCD	2008-08-11	2.5
boao090528-17	BOAO 1.8	CCD	2009-05-28	2.0
kore090529-16	BOAO 1.8	CCD	2009-05-29	2.4
mcao090513-01	MCAO 0.6	CCD	2009-05-13	2.4
mcao090519-03	MCAO 0.6	CCD	2009-05-19	3.2
mcao090520-01	MCAO 0.6	CCD	2009-05-20	4.8
mcao090521-01	MCAO 0.6	CCD	2009-05-21	4.9
mcao090522-01	MCAO 0.6	CCD	2009-05-22	3.1
mcao090531-02	MCAO 0.6	CCD	2009-05-31	2.1
mcao090601-01	MCAO 0.6	CCD	2009-06-01	3.3
mole090526-20	Moletai 1.65	CCD	2009-05-26	3.7
suho090520-19	Suhora 0.6	CCD	2009-05-20	2.2
suho090521-19	Suhora 0.6	CCD	2009-05-21	5.1
vien090525-19	Vienna 0.6	CCD	2009-05-25	6.2
krak100523-20	Krakow 0.4	CCD	2010-05-23	3.4
krak100526-20	Krakow 0.4	CCD	2010-05-26	2.3
krak100616-20	Krakow 0.4	CCD	2010-06-16	4.3
krak100617-20	Krakow 0.4	CCD	2010-06-17	4.5
mcao100516-01	MCAO 0.6	CCD	2010-05-16	2.0
mcao100521-01	MCAO 0.6	CCD	2010-05-21	0.9
mcao100521-05	MCAO 0.6	CCD	2010-05-21	0.8
mcao100526-01	MCAO 0.6	CCD	2010-05-26	3.3
mcd0100517-06	McDonald 2.1	CCD	2010-05-17	4.8

Table 1—Continued

Run Name	Telescope	Detector	Date	Length (hrs)
mole100516-22	Moletai 1.65	CCD	2010-05-26	1.8
mole100517-22	Moletai 1.65	CCD	2010-05-17	2.0
mole100520-21	Moletai 1.65	CCD	2010-05-20	3.3
mole100521-21	Moletai 1.65	CCD	2010-05-21	3.5
pjmo100519-04	PJMO 0.6	CCD	2010-05-19	4.0
pjmo100520-02	PJMO 0.6	CCD	2010-05-20	3.8
pjmo100521-05	PJMO 0.6	CCD	2010-05-21	3.3
pjmo100522-02	PJMO 0.6	CCD	2010-05-22	7.0
pjmo100523-04	PJMO 0.6	CCD	2010-05-23	6.0
pjmo100524-02	PJMO 0.6	CCD	2010-05-24	7.5
pjmo100527-02	PJMO 0.6	CCD	2010-05-27	8.3
pjmo100528-02	PJMO 0.6	CCD	2010-05-28	8.3
pjmo100619-03	PJMO 0.6	CCD	2010-06-19	4.0
pjmo100622-02	PJMO 0.6	CCD	2010-06-22	0.7
suho100617-21	Suhora 0.6	CCD	2010-06-17	4.3
terb100516-17	Terskol 2.0	CCD	2010-05-16	2.4
terb100520-17	Terskol 2.0	CCD	2010-05-20	8.9
terb100521-20	Terskol 2.0	CCD	2010-05-21	4.0
terb100524-19	Terskol 2.0	CCD	2010-05-24	5.6
terb100525-17	Terskol 2.0	CCD	2010-05-25	7.3
tueb100522-20	Tuebingen 0.8	SBig	2010-05-22	5.9
tueb100523-20	Tuebingen 0.8	SBig	2010-05-23	5.9
tueb100524-20	Tuebingen 0.8	SBig	2010-05-24	6.0
tueb100604-20	Tuebingen 0.8	SBig	2010-06-04	5.8
tueb100605-20	Tuebingen 0.8	SBig	2010-06-05	5.3
turk100512-18	Canakkale 1.2	CCD	2010-05-12	6.6
turk100513-22	Canakkale 1.2	CCD	2010-05-13	2.8
turk100516-19	Canakkale 1.2	CCD	2010-05-16	6.4
turk100520-19	Canakkale 1.2	CCD	2010-05-20	1.1
turk100522-21	Canakkale 1.2	CCD	2010-05-22	2.6
turk100523-19	Canakkale 1.2	CCD	2010-05-23	6.0
turk100611-19	Canakkale 1.2	CCD	2010-06-11	5.2

Table 1—Continued

Run Name	Telescope	Detector	Date	Length (hrs)
turk100613-19	Canakkale 1.2	CCD	2010-06-13	5.3
turk100615-20	Canakkale 1.2	CCD	2010-06-15	4.8
turk100618-19	Canakkale 1.2	CCD	2010-06-18	4.5
turk100620-20	Canakkale 1.2	CCD	2010-06-20	4.8
hvar110521-22	Hvar 1.0	CCD	2011-05-21	2.6
hvar110526-19	Hvar 1.0	CCD	2011-05-26	6.6
hvar110527-19	Hvar 1.0	CCD	2011-05-27	3.5
hvar110529-19	Hvar 1.0	CCD	2011-05-29	6.7
hvar110531-19	Hvar 1.0	CCD	2011-05-31	4.3
hvar110602-19	Hvar 1.0	CCD	2011-06-02	3.8
hvar110604-19	Hvar 1.0	CCD	2011-06-04	6.6
hvar110606-20	Hvar 1.0	CCD	2011-06-06	4.4
krak110506-20	Krakow 0.4	CCD	2011-05-06	5.4
krak110509-19	Krakow 0.4	CCD	2011-05-09	6.7
krak110510-19	Krakow 0.4	CCD	2011-05-10	6.2
krak110511-19	Krakow 0.4	CCD	2011-05-11	6.7
krak110512-19	Krakow 0.4	CCD	2011-05-12	3.1
krak110516-19	Krakow 0.4	CCD	2011-05-16	6.1
krak110517-19	Krakow 0.4	CCD	2011-05-17	5.6
krak110518-19	Krakow 0.4	CCD	2011-05-18	5.7
krak110519-20	Krakow 0.4	CCD	2011-05-19	5.4
krak110520-20	Krakow 0.4	CCD	2011-05-20	5.2
krak110522-21	Krakow 0.4	CCD	2011-05-22	4.3
krak110523-23	Krakow 0.4	CCD	2011-05-23	1.4
krak110524-19	Krakow 0.4	CCD	2011-05-24	4.0
krak110525-20	Krakow 0.4	CCD	2011-05-25	5.4
krak110526-20	Krakow 0.4	CCD	2011-05-26	5.3
krak110529-20	Krakow 0.4	CCD	2011-05-29	5.0
krak110530-20	Krakow 0.4	CCD	2011-05-30	4.8
krak110531-20	Krakow 0.4	CCD	2011-05-31	0.8
krak110604-20	Krakow 0.4	CCD	2011-06-04	5.3
mole110426-22	Moletai 1.65	CCD	2011-04-26	1.7

Table 1—Continued

Run Name	Telescope	Detector	Date	Length (hrs)
mole110427-21	Moletai 1.65	CCD	2011-04-27	3.7
mole110430-20	Moletai 1.65	CCD	2011-04-30	0.8
mole110502-20	Moletai 1.65	CCD	2011-05-02	0.4
mole110502-21	Moletai 1.65	CCD	2011-05-02	2.6
mole110505-20	Moletai 1.65	CCD	2011-05-05	1.1
mole110510-21	Moletai 1.65	CCD	2011-05-10	3.5
mtlm110426-05	Mt. Lemmon 1.0	CCD	2011-04-26	6.3
mtlm110427-06	Mt. Lemmon 1.0	CCD	2011-04-27	5.5
mtlm110428-04	Mt. Lemmon 1.0	CCD	2011-04-28	7.1
mtlm110429-05	Mt. Lemmon 1.0	CCD	2011-04-29	6.8
mtlm110430-05	Mt. Lemmon 1.0	CCD	2011-04-30	6.4
mtlm110501-05	Mt. Lemmon 1.0	CCD	2011-05-01	6.6
mtlm110502-05	Mt. Lemmon 1.0	CCD	2011-05-02	6.5
naoc110426-13	NAOC 0.5	CCD	2011-04-26	6.9
naoc110427-11	NAOC 0.5	CCD	2011-04-27	3.3
naos110426-13	NAOC 0.85	CCD	2011-04-26	6.9
naos110427-11	NAOC 0.85	CCD	2011-04-27	3.3
naos110428-12	NAOC 0.85	CCD	2011-04-28	2.6
naos110501-13	NAOC 0.85	CCD	2011-05-01	7.1
naos110502-12	NAOC 0.85	CCD	2011-05-02	8.3
naos110505-13	NAOC 0.85	CCD	2011-05-05	7.0
pjmo110426-07	PJMO 0.6	CCD	2011-04-26	3.0
pjmo110428-04	PJMO 0.6	CCD	2011-04-28	2.0
pjmo110429-03	PJMO 0.6	CCD	2011-04-29	2.5
pjmo110430-04	PJMO 0.6	CCD	2011-04-30	3.0
pjmo110503-04	PJMO 0.6	CCD	2011-05-03	2.6
pjmo110518-03	PJMO 0.6	CCD	2011-05-18	6.7
pjmo110519-03	PJMO 0.6	CCD	2011-05-19	2.7
pjmo110521-03	PJMO 0.6	CCD	2011-05-21	2.7
pjmo110524-02	PJMO 0.6	CCD	2011-05-24	5.2
pjmo110525-07	PJMO 0.6	CCD	2011-05-25	3.2
pjmo110526-03	PJMO 0.6	CCD	2011-05-26	7.0

Table 1—Continued

Run Name	Telescope	Detector	Date	Length (hrs)
pjmo110527-02	PJMO 0.6	CCD	2011-05-27	0.8
pjmo110527-03	PJMO 0.6	CCD	2011-05-27	6.7
suho110521-20	Suhora 0.6	CCD	2011-05-21	5.2
suho110522-19	Suhora 0.6	CCD	2011-05-22	5.9
suho110523-20	Suhora 0.6	CCD	2011-05-23	5.6
suho110527-20	Suhora 0.6	CCD	2011-05-27	2.0
suho110529-20	Suhora 0.6	CCD	2011-05-29	4.6
suho110530-20	Suhora 0.6	CCD	2011-05-30	4.9
terb110527-20	Terskol 2.0	CCD	2011-05-27	2.4
terb110529-17	Terskol 2.0	CCD	2011-05-27	4.4
terb110530-18	Terskol 2.0	CCD	2011-05-30	2.6
terb110531-17	Terskol 2.0	CCD	2011-05-31	1.8
terb110601-19	Terskol 2.0	CCD	2011-06-01	3.3
tueb110504-19	Tuebingen 0.8	SBig	2011-05-04	6.8
tueb110505-19	Tuebingen 0.8	SBig	2011-05-05	6.8
tueb110506-19	Tuebingen 0.8	SBig	2011-05-06	6.7
tueb110508-19	Tuebingen 0.8	SBig	2011-05-08	6.6
tueb110509-19	Tuebingen 0.8	SBig	2011-05-09	6.7
tueb110513-19	Tuebingen 0.8	SBig	2011-05-13	2.2
tueb110518-22	Tuebingen 0.8	SBig	2011-05-18	4.1
tueb110523-20	Tuebingen 0.8	SBig	2011-05-23	5.9
tueb110524-20	Tuebingen 0.8	SBig	2011-05-24	5.9
tueb110525-20	Tuebingen 0.8	SBig	2011-05-24	6.0
tueb110529-20	Tuebingen 0.8	SBig	2011-05-29	5.9
tueb110530-20	Tuebingen 0.8	SBig	2011-05-30	3.4
tubi110602-00	Tubitak 1.0	CCD	2011-06-02	1.1
tubi110602-23	Tubitak 1.0	CCD	2011-06-02	2.0
tubi110603-20	Tubitak 1.0	CCD	2011-06-03	5.2
boao120418-18	BOAO 1.8	CCD	2012-04-18	1.7
krak120418-00	Krakow 0.4	CCD	2012-04-18	1.8
krak120421-00	Krakow 0.4	CCD	2012-04-21	4.6
krak120423-00	Krakow 0.4	CCD	2012-04-23	1.7

Table 1—Continued

Run Name	Telescope	Detector	Date	Length (hrs)
krak120428-00	Krakow 0.4	CCD	2012-04-28	6.6
krak120429-00	Krakow 0.4	CCD	2012-04-29	6.1
krak120430-00	Krakow 0.4	CCD	2012-04-30	6.7
mtlm120419-10	Mt. Lemmon 1.0	CCD	2012-04-19	1.7
mtlm120420-10	Mt. Lemmon 1.0	CCD	2012-04-20	1.4
mtlm120421-05	Mt. Lemmon 1.0	CCD	2012-04-21	6.2
mtlm120422-07	Mt. Lemmon 1.0	CCD	2012-04-22	4.8
na50120524-12	NAOC 0.5	CCD	2012-05-24	4.5
na50120525-12	NAOC 0.5	CCD	2012-05-25	4.4
na50120526-14	NAOC 0.5	CCD	2012-05-26	3.3
na50120527-12	NAOC 0.5	CCD	2012-05-27	4.9
na50120530-13	NAOC 0.5	CCD	2012-05-30	6.0
pjmo120425-03	PJMO 0.6	CCD	2012-04-25	7.2
pjmo120426-03	PJMO 0.6	CCD	2012-04-26	4.3
prom120430-04	PROMPT 0.4	CCD	2012-04-30	2.2
prom120430-07	PROMPT 0.4	CCD	2012-04-30	1.1
prom120501-04	PROMPT 0.4	CCD	2012-05-01	4.5
prom120502-04	PROMPT 0.4	CCD	2012-05-02	4.4
prom120503-04	PROMPT 0.4	CCD	2012-05-03	0.9
prom120504-04	PROMPT 0.4	CCD	2012-05-04	4.5
prom120509-04	PROMPT 0.4	CCD	2012-05-09	4.3
prom120510-04	PROMPT 0.4	CCD	2012-05-10	4.1
prom120511-03	PROMPT 0.4	CCD	2012-05-11	4.1
prom120512-03	PROMPT 0.4	CCD	2012-05-12	4.0
prom120513-03	PROMPT 0.4	CCD	2012-05-13	2.1
prom120514-03	PROMPT 0.4	CCD	2012-05-14	4.0
prom120515-03	PROMPT 0.4	CCD	2012-05-15	4.0
suho120501-20	Suhora 0.6	CCD	2012-05-01	6.0
suho120502-21	Suhora 0.6	CCD	2012-05-02	5.1
suho120503-23	Suhora 0.6	CCD	2012-05-03	2.4
suho120505-19	Suhora 0.6	CCD	2012-05-05	2.1
tubi120420-01	Tubitak 1.0	CCD	2012-04-20	1.0

Table 1—Continued

Run Name	Telescope	Detector	Date	Length (hrs)
tubi120423-19	Tubitak 1.0	CCD	2012-04-23	6.6
tubi120512-20	Tubitak 1.0	CCD	2012-04-23	5.2
caam130412-21	Cannakkale 1.2	CCD	2013-04-12	4.0
caam130417-21	Cannakkale 1.2	CCD	2013-04-17	3.2
caam130418-21	Cannakkale 1.2	CCD	2013-04-18	4.5
krak130418-00	Krakow 0.4	CCD	2013-04-18	6.7
krak130421-00	Krakow 0.4	CCD	2013-04-18	7.4
krak130425-00	Krakow 0.4	CCD	2013-04-25	6.7
krak130426-00	Krakow 0.4	CCD	2013-04-26	2.1
naos130503-13	NAOC 0.85	CCD	2013-05-03	6.0
pjmo130429-06	PJMO 0.6	CCD	2013-04-29	2.7
pjmo130430-07	PJMO 0.6	CCD	2013-04-30	2.1
pjmo130503-07	PJMO 0.6	CCD	2013-05-03	3.6
pjmo130505-04	PJMO 0.6	CCD	2013-05-05	6.8
suho130422-21	Suhora 0.6	CCD	2013-04-22	4.6
suho130425-20	Suhora 0.6	CCD	2013-04-25	5.9
suho130426-20	Suhora 0.6	CCD	2013-04-26	5.4
suho130501-19	Suhora 0.6	CCD	2013-05-01	6.1
suho130504-21	Suhora 0.6	CCD	2013-05-04	4.4
suho130505-19	Suhora 0.6	CCD	2013-05-05	5.5
caam140610-19	Cannakkale 1.2	CCD	2014-06-10	5.5
krak140530-21	Krakow 0.4	CCD	2014-05-30	2.4
krak140604-20	Krakow 0.4	CCD	2014-06-04	5.5
krak140606-20	Krakow 0.4	CCD	2014-06-06	4.7
krak140607-20	Krakow 0.4	CCD	2014-06-07	5.1
krak140608-20	Krakow 0.4	CCD	2014-06-08	5.2
krak140609-19	Krakow 0.4	CCD	2014-06-09	4.7
krak140610-20	Krakow 0.4	CCD	2014-06-10	2.4
mcao140602-05	MCAO 0.6	CCD	2014-06-02	3.0
mcao140603-01	MCAO 0.6	CCD	2014-06-03	4.1
mcao140607-01	MCAO 0.6	CCD	2014-06-07	4.0
mcao140608-01	MCAO 0.6	CCD	2014-06-08	3.9

Table 1—Continued

Run Name	Telescope	Detector	Date	Length (hrs)
mole140526-20	Moletai 1.65	CCD	2014-05-26	2.5
mole140527-20	Moletai 1.65	CCD	2014-05-27	3.7
mole140605-20	Moletai 1.65	CCD	2014-06-05	3.3
mole140607-20	Moletai 1.65	CCD	2014-06-07	2.9
naos140605-15	NAOC 0.85	CCD	2014-06-05	5.7
naos140606-17	NAOC 0.85	CCD	2014-06-06	3.9
pjmo140519-04	PJMO 0.6	CCD	2014-05-19	4.0
pjmo140529-03	PJMO 0.6	CCD	2014-05-29	5.4
pjmo140530-03	PJMO 0.6	CCD	2014-05-30	4.3
pjmo140531-02	PJMO 0.6	CCD	2014-05-31	5.0
pjmo140601-03	PJMO 0.6	CCD	2014-06-01	3.3
pjmo140602-02	PJMO 0.6	CCD	2014-06-02	4.5
pjmo140603-02	PJMO 0.6	CCD	2014-06-03	7.1
pjmo140604-04	PJMO 0.6	CCD	2014-06-04	5.8
pjmo140611-03	PJMO 0.6	CCD	2014-06-11	5.9
suho140604-19	Suhora 0.6	CCD	2014-06-04	4.4
suho140606-20	Suhora 0.6	CCD	2014-06-06	4.7
ters140604-20	Terskol 0.6	CCD	2014-06-04	2.0
ters140619-20	Terskol 0.6	CCD	2014-06-19	6.0
tsao140524-17	Tien Shan 1.0	CCD	2014-05-24	4.7
tsao140525-16	Tien Shan 1.0	CCD	2014-05-25	6.0
tsao140610-15	Tien Shan 1.0	CCD	2014-06-10	1.0
tsao140611-16	Tien Shan 1.0	CCD	2014-06-11	6.0
tsao140613-17	Tien Shan 1.0	CCD	2014-06-13	4.6
tsao140616-19	Tien Shan 1.0	CCD	2014-06-16	1.4
tsao140619-17	Tien Shan 1.0	CCD	2014-06-19	4.8
tsao140620-18	Tien Shan 1.0	CCD	2014-06-20	3.1
tsao140627-16	Tien Shan 1.0	CCD	2014-06-27	5.9
tsao140628-16	Tien Shan 1.0	CCD	2014-06-28	5.9
krak150420-20	Krakow 0.4	CCD	2015-05-20	2.1
krak150421-19	Krakow 0.4	CCD	2015-05-21	7.5
pjmo150420-03	PJMO 0.6	CCD	2015-04-20	7.3

Table 1—Continued

Run Name	Telescope	Detector	Date	Length (hrs)
pjmo150421-05	PJMO 0.6	CCD	2015-04-21	5.4
pjmo150422-03	PJMO 0.6	CCD	2015-04-22	4.7
pjmo150426-03	PJMO 0.6	CCD	2015-04-26	7.4
prom150428-08	PROMPT 0.4	CCD	2015-04-28	6.5
prom150429-03	PROMPT 0.4	CCD	2015-04-29	6.6
prom150501-03	PROMPT 0.4	CCD	2015-05-01	6.2

Table 2. 1982-2006 Detected Independent Frequencies

Frequency μHz	Period s	Amplitude mma	Signal/Noise
1982			
1236.483 ± 0.07	808.75	16.70 ± 0.06	9.4
1431.112 ± 0.04	698.76	30.86 ± 0.06	11.4
1613.842 ± 0.05	619.65	26.12 ± 0.06	9.7
1618.845 ± 0.06	617.72	29.34 ± 0.06	10.9
2368.563 ± 0.10	422.20	12.52 ± 0.06	5.8
1984			
1124.701 ± 3.5	889.13	24.7 ± 1.1	7.2
1626.474 ± 3.5	614.83	25.9 ± 1.1	6.8
1985			
1166.944 ± 0.05	856.94	6.43 ± 0.06	11
1176.489 ± 0.03	849.99	35.70 ± 0.06	16.0
1614.554 ± 0.04	619.37	9.15 ± 0.06	4.6
2351.762 ± 0.04	425.22	14.34 ± 0.06	12
1986			
1081.025 ± 0.03	925.05	5.1 ± 0.4	4.6
1160.678 ± 0.03	861.57	4.9 ± 0.4	4.5
1223.803 ± 0.02	817.12	9.3 ± 0.4	9.1
1233.585 ± 0.01	810.65	14.9 ± 0.4	14.5
1385.240 ± 0.03	721.90	6.7 ± 0.4	6.4
1426.181 ± 0.01	701.17	14.2 ± 0.4	14.3
1525.030 ± 0.01	655.72	21.3 ± 0.4	21.4
1611.691 ± 0.01	620.47	20.9 ± 0.4	20.9

Table 2—Continued

Frequency μHz	Period s	Amplitude mma	Signal/Noise
2157.783 ± 0.04	463.44	2.4 ± 0.4	4
2165.564 ± 0.03	461.77	4.8 ± 0.4	4
2368.938 ± 0.03	422.13	5.8 ± 0.4	5.6
1990			
1112.933 ± 0.03	898.53	2.31 ± 0.32	4.0
1114.180 ± 0.03	897.52	2.44 ± 0.32	4.1
1118.324 ± 0.02	894.20	5.24 ± 0.32	8.9
1119.089 ± 0.03	893.58	2.83 ± 0.32	4.8
1224.216 ± 0.03	816.83	22.17 ± 0.32	4.0
1233.413 ± 0.03	810.76	4.80 ± 0.32	8.4
1245.395 ± 0.03	802.96	2.17 ± 0.32	4.0
1288.995 ± 0.03	775.80	3.50 ± 0.32	6.3
1291.229 ± 0.03	774.46	4.31 ± 0.32	7.6
1295.400 ± 0.03	771.96	3.27 ± 0.32	5.8
1297.540 ± 0.01	770.69	14.76 ± 0.32	26.1
1304.075 ± 0.03	766.83	4.67 ± 0.32	8.3
1355.447 ± 0.03	737.76	2.20 ± 0.32	4.0
1361.728 ± 0.03	734.36	2.90 ± 0.32	5.2
1368.588 ± 0.03	730.68	3.32 ± 0.32	5.9
1375.434 ± 0.03	727.04	3.18 ± 0.32	5.7
1421.041 ± 0.02	703.71	8.22 ± 0.32	15.1
1423.704 ± 0.03	702.39	3.11 ± 0.32	5.8
1427.365 ± 0.01	700.59	19.39 ± 0.32	35.8
1428.663 ± 0.03	699.96	2.61 ± 0.32	4.8
1433.729 ± 0.02	697.48	7.29 ± 0.32	13.5
1435.209 ± 0.03	696.76	3.50 ± 0.32	6.5
1512.798 ± 0.02	661.03	5.57 ± 0.32	10.7
1518.661 ± 0.02	658.47	8.34 ± 0.32	15.9

Table 2—Continued

Frequency μHz	Period s	Amplitude mma	Signal/Noise
1519.372 ± 0.02	658.17	5.88 ± 0.32	11.2
1524.924 ± 0.02	655.77	5.98 ± 0.32	11.2
1525.498 ± 0.02	655.52	6.95 ± 0.32	13.0
1611.741 ± 0.02	620.45	6.09 ± 0.32	12.3
1617.380 ± 0.03	618.28	4.69 ± 0.32	9.7
1623.709 ± 0.02	615.87	5.04 ± 0.32	10.2
2154.009 ± 0.03	464.25	4.40 ± 0.32	11.2
2157.765 ± 0.03	463.44	2.27 ± 0.32	5.8
2358.946 ± 0.02	423.92	5.63 ± 0.32	14.1
2362.507 ± 0.02	423.28	5.71 ± 0.32	14.3
2366.408 ± 0.03	422.58	4.59 ± 0.32	11.5
1991			
1296.087 ± 0.13	771.55	10.11 ± 0.41	17.7
1296.577 ± 0.13	771.26	18.25 ± 0.41	29.8
1308.777 ± 0.05	764.07	5.02 ± 0.41	9.9
1396.945 ± 0.05	715.85	3.95 ± 0.41	8.4
1419.934 ± 0.01	704.26	29.3 ± 0.41	45.6
1423.333 ± 0.04	702.58	5.23 ± 0.41	6.3
1427.062 ± 0.04	700.74	5.02 ± 0.41	7.4
1443.381 ± 0.05	692.82	4.81 ± 0.41	9.7
2150.307 ± 0.05	465.05	2.36 ± 0.41	4.1
2154.389 ± 0.05	464.17	2.79 ± 0.41	4.6
2157.939 ± 0.05	463.41	2.62 ± 0.41	4.4
2370.121 ± 0.04	421.92	5.01 ± 0.41	9.2
2374.211 ± 0.05	421.19	3.26 ± 0.41	5.7
2378.195 ± 0.04	420.49	5.58 ± 0.41	10.7
1992			

Table 2—Continued

Frequency μHz	Period s	Amplitude mma	Signal/Noise
1035.357 ± 0.05	965.85	7.35 ± 0.31	4.1
1101.952 ± 0.05	907.48	6.40 ± 0.31	3.7
1195.349 ± 0.003	836.58	6.90 ± 0.31	4.1
1233.263 ± 0.001	810.86	20.79 ± 0.31	13.5
1242.854 ± 0.003	804.60	14.20 ± 0.31	8.8
1265.279 ± 0.003	790.34	12.25 ± 0.31	7.1
1420.845 ± 0.001	703.81	20.59 ± 0.31	13.1
1438.411 ± 0.003	695.21	17.71 ± 0.31	11.9
1622.795 ± 0.003	616.22	14.26 ± 0.31	9.2
1628.812 ± 0.004	613.94	10.9 ± 0.317	6.5
2162.104 ± 0.007	462.51	4.26 ± 0.31	4.2
2166.094 ± 0.007	461.66	5.66 ± 0.31	4.8
2351.041 ± 0.007	425.34	6.75 ± 0.31	5.2
2359.162 ± 0.007	423.88	6.55 ± 0.31	9.2
2366.443 ± 0.007	422.58	7.17 ± 0.31	6.3
1994			
939.264 ± 0.007	1064.66	2.36 ± 0.10	5.7
1024.773 ± 0.011	975.83	3.46 ± 0.10	8.8
1064.931 ± 0.012	939.03	2.82 ± 0.10	7.4
1106.833 ± 0.013	903.48	2.56 ± 0.10	7.0
1113.548 ± 0.012	898.03	3.95 ± 0.10	9.4
1164.637 ± 0.012	858.64	3.12 ± 0.10	8.6
1176.684 ± 0.013	849.85	2.79 ± 0.10	7.2
1224.306 ± 0.012	816.79	3.28 ± 0.10	9.1
1234.488 ± 0.013	810.05	2.70 ± 0.10	7.7
1235.491 ± 0.005	809.39	13.13 ± 0.10	37.3
1242.357 ± 0.013	804.92	3.33 ± 0.10	9.1

Table 2—Continued

Frequency μHz	Period s	Amplitude mma	Signal/Noise
1246.494 ± 0.013	802.25	2.69 ± 0.10	7.8
1286.550 ± 0.003	777.27	9.45 ± 0.10	27.6
1291.023 ± 0.009	774.58	6.07 ± 0.10	17.8
1293.244 ± 0.009	773.25	5.85 ± 0.10	16.1
1297.737 ± 0.005	770.57	21.5 ± 0.10	61.9
1298.710 ± 0.010	769.99	4.45 ± 0.10	12.5
1304.464 ± 0.009	766.64	6.84 ± 0.10	19.9
1305.352 ± 0.013	766.08	2.54 ± 0.10	7.0
1309.003 ± 0.013	763.94	2.76 ± 0.10	8.4
1312.045 ± 0.013	762.17	2.67 ± 0.10	7.9
1419.641 ± 0.003	704.40	18.70 ± 0.10	54.4
1422.947 ± 0.013	702.77	2.86 ± 0.10	8.2
1426.395 ± 0.003	701.07	16.05 ± 0.10	46.6
1430.851 ± 0.005	698.88	10.35 ± 0.10	30.1
1433.167 ± 0.010	697.75	4.06 ± 0.10	11.6
1437.607 ± 0.006	695.60	8.28 ± 0.10	24.1
1438.523 ± 0.011	695.16	3.68 ± 0.10	10.7
1440.997 ± 0.012	693.96	2.48 ± 0.10	7.2
1441.910 ± 0.009	693.52	4.09 ± 0.10	11.9
1611.351 ± 0.009	620.60	5.12 ± 0.10	14.2
1617.450 ± 0.010	618.26	3.61 ± 0.10	9.5
1618.545 ± 0.009	617.84	4.04 ± 0.10	11.2
1624.624 ± 0.009	615.53	5.83 ± 0.10	16.1
1625.634 ± 0.009	615.14	4.89 ± 0.10	13.9
2150.498 ± 0.010	465.01	3.22 ± 0.10	9.4
2154.130 ± 0.010	464.22	4.75 ± 0.10	13.7
2157.844 ± 0.012	463.43	2.70 ± 0.10	7.6
2358.880 ± 0.010	423.93	4.53 ± 0.10	13.5
2362.636 ± 0.005	423.26	9.29 ± 0.10	31.2
2366.505 ± 0.011	422.56	4.26 ± 0.10	13.2

Table 2—Continued

Frequency μHz	Period s	Amplitude mma	Signal/Noise
1996			
937.695 ± 0.028	1066.44	4.27 ± 0.28	3.5
1024.276 ± 0.028	976.30	6.78 ± 0.28	6.4
1104.483 ± 0.025	905.40	5.55 ± 0.28	5.1
1178.461 ± 0.025	848.56	5.34 ± 0.28	5.5
1227.936 ± 0.022	814.37	7.66 ± 0.28	7.5
1233.14 ± 0.015	810.94	13.50 ± 0.28	12.1
1234.506 ± 0.015	810.04	12.53 ± 0.28	11.2
1247.959 ± 0.022	801.31	7.84 ± 0.28	4.1
1261.275 ± 0.015	792.85	11.08 ± 0.28	11.6
1291.169 ± 0.015	774.49	10.71 ± 0.28	9.7
1294.899 ± 0.025	772.26	6.95 ± 0.28	7.9
1297.194 ± 0.010	770.89	22.05 ± 0.28	2.4
1420.057 ± 0.010	704.20	20.26 ± 0.28	19.7
1426.443 ± 0.010	701.04	18.41 ± 0.28	8.3
1430.253 ± 0.012	699.18	13.15 ± 0.28	12.8
1436.261 ± 0.022	696.25	8.20 ± 0.28	9.1
1628.296 ± 0.028	614.14	6.13 ± 0.28	6.3
2154.117 ± 0.028	464.23	7.40 ± 0.28	7.1
2358.806 ± 0.025	423.94	6.01 ± 0.28	4.7
2362.617 ± 0.014	423.26	9.87 ± 0.28	9.0
2367.288 ± 0.025	422.42	8.92 ± 0.28	11.6
2000			
938.991 ± 0.015	1064.95	3.09 ± 0.01	9.4
946.238 ± 0.015	1056.82	1.20 ± 0.01	4.0
1110.999 ± 0.015	900.09	1.98 ± 0.01	7.0

Table 2—Continued

Frequency μHz	Period s	Amplitude mma	Signal/Noise
1171.564 ± 0.015	853.56	1.89 ± 0.01	7.0
1173.021 ± 0.012	852.50	2.32 ± 0.01	8.8
1251.851 ± 0.004	798.82	3.21 ± 0.01	12.5
1254.503 ± 0.002	797.13	8.60 ± 0.01	33.1
1255.583 ± 0.002	796.44	14.72 ± 0.01	67.1
1256.248 ± 0.005	796.02	8.04 ± 0.01	42.6
1257.268 ± 0.010	795.38	3.05 ± 0.01	15.2
1258.288 ± 0.010	794.73	2.06 ± 0.01	5.7
1296.603 ± 0.001	771.25	28.08 ± 0.01	109.5
1378.795 ± 0.008	725.27	4.33 ± 0.01	17.3
1379.737 ± 0.010	724.78	2.64 ± 0.01	10.4
1420.101 ± 0.001	704.18	29.78 ± 0.01	118.8
1423.597 ± 0.010	702.45	3.08 ± 0.01	12.3
1736.660 ± 0.014	575.82	1.02 ± 0.01	4.0
2150.515 ± 0.013	465.01	2.99 ± 0.01	11.2
2154.040 ± 0.013	464.24	5.38 ± 0.01	19.9
2157.736 ± 0.012	463.45	2.51 ± 0.01	9.5
2359.118 ± 0.008	423.89	5.51 ± 0.01	23.7
2366.271 ± 0.010	422.61	5.90 ± 0.01	25.1
2006			
923.976 ± 0.001	1082.28	1.43 ± 0.01	5.2
938.216 ± 0.002	1065.85	1.23 ± 0.01	4.4
1024.496 ± 0.002	976.09	1.44 ± 0.01	4.8
1033.760 ± 0.002	967.34	1.85 ± 0.01	6.9
1039.075 ± 0.001	962.39	7.95 ± 0.01	27.2
1039.474 ± 0.001	962.02	2.84 ± 0.01	9.7
1041.535 ± 0.001	960.12	1.18 ± 0.01	4.3
1044.381 ± 0.002	957.50	1.63 ± 0.01	6.2

Table 2—Continued

Frequency μHz	Period s	Amplitude mma	Signal/Noise
1113.582 ± 0.001	898.02	2.71 ± 0.01	9.4
1120.404 ± 0.001	892.53	2.09 ± 0.01	7.3
1120.902 ± 0.001	892.14	2.98 ± 0.01	10.2
1121.704 ± 0.002	891.50	1.26 ± 0.01	4.4
1130.144 ± 0.002	884.84	1.91 ± 0.01	7.3
1161.552 ± 0.001	860.92	2.74 ± 0.01	9.6
1173.015 ± 0.001	852.50	7.26 ± 0.01	25.4
1178.096 ± 0.002	848.83	1.13 ± 0.01	4.3
1184.470 ± 0.002	844.26	1.64 ± 0.01	6.2
1222.199 ± 0.002	818.20	1.72 ± 0.01	6.3
1222.751 ± 0.001	817.83	5.04 ± 0.01	18.3
1222.945 ± 0.001	817.70	4.59 ± 0.01	5.1
1228.185 ± 0.002	814.21	2.71 ± 0.01	9.4
1228.791 ± 0.001	813.81	5.27 ± 0.01	19.0
1234.124 ± 0.001	810.29	24.87 ± 0.01	88.0
1239.510 ± 0.001	806.77	5.07 ± 0.01	18.3
1240.237 ± 0.002	806.30	2.85 ± 0.01	9.9
1244.790 ± 0.002	803.35	1.90 ± 0.01	6.9
1245.219 ± 0.001	803.07	4.75 ± 0.01	17.1
1246.032 ± 0.001	802.55	4.44 ± 0.01	15.2
1421.012 ± 0.002	703.72	2.81 ± 0.01	7.1
1429.209 ± 0.001	699.69	5.65 ± 0.01	22.5
1512.141 ± 0.002	661.31	1.79 ± 0.01	6.4
1736.301 ± 0.001	575.94	16.38 ± 0.01	75.2
1737.962 ± 0.002	575.39	1.80 ± 0.01	7.6
1741.666 ± 0.001	574.16	11.01 ± 0.01	49.7
1743.733 ± 0.001	573.48	5.59 ± 0.01	8.4
1749.083 ± 0.001	571.73	11.88 ± 0.01	50.2
1856.845 ± 0.002	538.55	1.44 ± 0.01	6.4
2150.393 ± 0.001	465.03	4.06 ± 0.01	17.3

Table 2—Continued

Frequency μHz	Period s	Amplitude mma	Signal/Noise
2154.223 ± 0.001	464.20	5.50 ± 0.01	21.8
2158.073 ± 0.001	463.38	7.24 ± 0.01	29.0
2359.052 ± 0.001	423.90	5.94 ± 0.01	22.1
2363.058 ± 0.002	423.18	1.7 ± 0.011	6.0
2366.524 ± 0.001	422.56	6.31 ± 0.01	23.0

Table 3. 2007-2015 Detected Independent Frequencies

Frequency μHz	Period s	Amplitude mma	Signal/Noise
2007			
1088.951 ± 0.05	918.31	6.9 ± 0.7	5
1121.169 ± 0.04	891.93	10.19 ± 0.7	8
1233.956 ± 0.02	810.40	23 ± 0.7	20
1251.193 ± 0.05	799.24	9.56 ± 0.7	8
1735.444 ± 0.03	576.22	13.47 ± 0.7	13
2156.288 ± 0.03	463.76	7.26 ± 0.7	7
2008			
1235.745 ± 0.004	809.23	25.14 ± 0.33	23.9
1735.716 ± 0.004	576.13	21.77 ± 0.33	22.6
1741.459 ± 0.009	574.23	10.14 ± 0.33	9.8
1750.185 ± 0.012	571.37	4.47 ± 0.33	5.6
2150.245 ± 0.011	465.06	5.66 ± 0.33	7.7
2158.416 ± 0.01	463.30	11.07 ± 0.33	11
2358.895 ± 0.01	423.93	7.95 ± 0.33	10.2
2366.872 ± 0.01	422.50	7.93 ± 0.33	10.2
2009			
1088.445 ± 0.018	918.74	7.82 ± 0.28	9
1235.845 ± 0.007	809.16	9.64 ± 0.28	22.4
1236.849 ± 0.018	808.51	7.91 ± 0.28	9.1
1300.029 ± 0.018	576.29	4.10 ± 0.28	4.7
1735.699 ± 0.006	576.14	20.60 ± 0.28	22.8
1741.415 ± 0.018	574.25	7.15 ± 0.28	8.8
1750.525 ± 0.012	571.26	5.98 ± 0.28	6.8
2150.261 ± 0.014	465.06	5.22 ± 0.28	6.5

Table 3—Continued

Frequency μHz	Period s	Amplitude mma	Signal/Noise
2158.474 ± 0.003	463.29	10.72 ± 0.28	13.4
2358.952 ± 0.026	423.92	5.89 ± 0.28	8.1
2366.893 ± 0.018	422.49	7.28 ± 0.28	10.1
2010			
1087.790 ± 0.024	919.29	2.47 ± 0.15	5.1
1104.397 ± 0.023	891.34	2.57 ± 0.15	5.1
1112.868 ± 0.009	898.58	6.22 ± 0.15	13.2
1121.901 ± 0.005	891.34	12.6 ± 0.15	26.6
1122.674 ± 0.021	889.89	2.73 ± 0.15	5.2
1123.731 ± 0.020	891.33	3.31 ± 0.15	7.1
1200.999 ± 0.017	832.64	3.33 ± 0.15	7.1
1211.906 ± 0.021	825.15	2.99 ± 0.15	6.4
1236.278 ± 0.003	808.88	18.9 ± 0.15	39.7
1237.011 ± 0.023	808.41	4.10 ± 0.15	9.2
1241.721 ± 0.014	805.33	3.32 ± 0.15	7.0
1299.274 ± 0.018	769.66	3.89 ± 0.15	7.6
1735.786 ± 0.003	576.11	21.72 ± 0.015	46.9
1741.367 ± 0.004	574.26	8.34 ± 0.15	17.2
1745.084 ± 0.025	573.04	2.53 ± 0.15	5.2
1750.642 ± 0.005	571.19	10.93 ± 0.15	25.2
1859.431 ± 0.023	537.80	2.50 ± 0.15	5.2
2008.645 ± 0.025	497.85	2.66 ± 0.15	5.2
2150.138 ± 0.025	465.09	4.52 ± 0.15	9.7
2154.432 ± 0.025	464.16	2.17 ± 0.15	5.1
2158.524 ± 0.006	463.28	9.95 ± 0.15	23.4
2358.818 ± 0.008	423.94	9.05 ± 0.15	23.1
2362.603 ± 0.017	423.26	3.19 ± 0.15	6.7
2366.990 ± 0.008	422.48	7.40 ± 0.15	19

Table 3—Continued

Frequency μHz	Period s	Amplitude mma	Signal/Noise
2011			
954.564 ± 0.008	1047.59	5.2 ± 0.17	10.9
954.922 ± 0.02	1047.21	4.22 ± 0.17	8.7
1113.07 ± 0.013	898.45	5.72 ± 0.17	11.6
1113.641 ± 0.02	897.96	3.2 ± 0.17	6.4
1235.415 ± 0.004	809.44	9.76 ± 0.17	20.1
1362.917 ± 0.03	733.72	1.66 ± 0.17	4.0
1511.537 ± 0.03	661.58	1.85 ± 0.17	4.3
1614.827 ± 0.016	619.26	4.40 ± 0.17	10.5
1735.871 ± 0.003	576.08	20.3 ± 0.17	150.5
1736.14 ± 0.037	575.99	4.70 ± 0.17	11.1
1747.123 ± 0.037	572.37	3.30 ± 0.17	7.9
1750.833 ± 0.013	571.16	3.77 ± 0.17	8.9
1856.872 ± 0.03	538.54	1.62 ± 0.17	3.8
2008.742 ± 0.02	497.82	3.00 ± 0.17	7.4
2150.138 ± 0.016	465.09	4.98 ± 0.17	13.4
2154.294 ± 0.028	464.19	3.73 ± 0.17	8.9
2158.571 ± 0.007	463.27	9.10 ± 0.17	24.6
2358.707 ± 0.009	423.96	7.63 ± 0.17	27.4
2359.911 ± 0.04	423.74	1.58 ± 0.17	2.47
$2366.986 \pm$	422.48	8.9 ± 0.17	26.4
2012			
1113.254 ± 0.014	898.27	4.1 ± 0.24	6.2
1161.469 ± 0.01	860.98	5.21 ± 0.24	7.7
1211.371 ± 0.006	825.51	9.89 ± 0.24	14.7
1212.822 ± 0.009	824.52	6.46 ± 0.24	9.6

Table 3—Continued

Frequency μHz	Period s	Amplitude mma	Signal/Noise
1213.995 ± 0.006	823.73	8.66 ± 0.24	12.8
1215.915 ± 0.01	822.43	5.72 ± 0.24	8.5
1222.598 ± 0.004	817.930	11.53 ± 0.24	17.2
1226.836 ± 0.008	815.11	6.89 ± 0.24	10.3
1233.355 ± 0.004	810.80	12.53 ± 0.24	18.6
1235.431 ± 0.009	809.43	6.70 ± 0.24	9.9
1246.397 ± 0.004	802.31	13.35 ± 0.24	19.9
1258.482 ± 0.009	794.61	6.26 ± 0.24	9.3
1723.487 ± 0.015	580.22	4.30 ± 0.24	6.1
1734.393 ± 0.006	576.57	8.54 ± 0.24	12.1
1735.975 ± 0.004	576.05	12.4 ± 0.24	17.7
1745.543 ± 0.012	572.89	4.44 ± 0.24	6.3
1747.152 ± 0.008	572.36	6.74 ± 0.24	9.5
1748.895 ± 0.009	571.79	6.36 ± 0.24	9.0
1750.345 ± 0.008	571.32	6.19 ± 0.24	8.9
2150.072 ± 0.02	465.10	2.74 ± 0.24	4.0
2155.981 ± 0.015	463.83	3.68 ± 0.24	5.2
2158.563 ± 0.006	463.27	8.86 ± 0.24	12.2
2181.89 ± 0.015	458.32	3.60 ± 0.24	4.9
2355.788 ± 0.01	424.47	5.48 ± 0.24	8.7
2358.721 ± 0.01	423.96	5.17 ± 0.24	8.4
2366.807 ± 0.009	422.51	5.67 ± 0.24	9.4
2372.715 ± 0.015	421.46	3.81 ± 0.24	6.2
2013			
1086.678 ± 0.007	920.24	5.28 ± 0.18	6.5
1097.639 ± 0.014	911.05	5.28 ± 0.18	5.4
1123.417 ± 0.023	890.14	4.46 ± 0.18	5.9
1235.981 ± 0.005	809.07	15.5 ± 0.18	15.0

Table 3—Continued

Frequency μHz	Period s	Amplitude mma	Signal/Noise
1241.938 ± 0.013	805.19	7.50 ± 0.18	6.4
1362.571 ± 0.027	733.91	4.74 ± 0.18	5.2
1614.872 ± 0.007	619.24	10.3 ± 0.18	10.2
1629.282 ± 0.015	613.77	4.80 ± 0.18	5.3
1736.468 ± 0.008	575.88	11.1 ± 0.18	11.4
1737.008 ± 0.008	575.70	11.2 ± 0.18	11.4
1746.007 ± 0.024	572.73	5.66 ± 0.18	5.7
2158.532 ± 0.006	463.28	8.32 ± 0.18	9.4
2162.432 ± 0.014	462.44	5.55 ± 0.18	6.4
2358.635 ± 0.007	423.97	7.50 ± 0.18	9.2
2364.019 ± 0.026	423.013	3.20 ± 0.18	6.4
2367.037 ± 0.014	422.47	6.82 ± 0.18	8.5
2014			
1023.122 ± 0.010	977.40	2.38 ± 0.17	6.1
1113.15 ± 0.008	898.35	3.53 ± 0.17	8.7
1158.561 ± 0.014	863.14	2.33 ± 0.17	6.0
1161.856 ± 0.008	860.69	3.33 ± 0.17	8.6
1171.782 ± 0.010	853.40	2.96 ± 0.17	8.0
1172.914 ± 0.011	852.58	2.20 ± 0.17	5.7
1221.633 ± 0.004	818.58	5.19 ± 0.17	13.6
1230.125 ± 0.008	812.93	3.11 ± 0.17	8.1
1234.599 ± 0.003	809.98	10.08 ± 0.17	26.4
1235.145 ± 0.001	809.62	8.63 ± 0.17	48.7
1236.228 ± 0.004	808.96	5.96 ± 0.17	15.6
1237.719 ± 0.001	807.94	9.60 ± 0.17	25.0
1248.182 ± 0.01	801.17	2.79 ± 0.17	7.3
1299.081 ± 0.003	769.77	10.58 ± 0.17	27.6
1311.786 ± 0.008	762.32	3.29 ± 0.17	8.5

Table 3—Continued

Frequency μHz	Period s	Amplitude mma	Signal/Noise
1312.442 ± 0.008	761.94	3.10 ± 0.17	8.3
1361.767 ± 0.018	734.34	1.61 ± 0.17	4.1
1371.106 ± 0.014	729.34	1.93 ± 0.17	5.0
1429.540 ± 0.009	699.53	2.97 ± 0.17	7.5
1511.465 ± 0.006	661.61	4.25 ± 0.17	10.2
1520.357 ± 0.018	657.74	1.53 ± 0.17	3.7
1633.117 ± 0.023	612.33	1.19 ± 0.17	2.7
1735.955 ± 0.001	576.05	18.4 ± 0.17	43.1
1739.822 ± 0.019	574.77	1.47 ± 0.17	3.5
1740.357 ± 0.012	574.59	2.22 ± 0.17	5.3
1741.406 ± 0.019	574.25	1.3 ± 0.17	3.3
2003.559 ± 0.009	499.11	1.9 ± 0.17	4.4
2008.717 ± 0.018	497.83	1.53 ± 0.17	3.5
2150.280 ± 0.010	465.06	2.78 ± 0.17	6.7
2154.315 ± 0.012	464.18	2.55 ± 0.17	6.1
2158.634 ± 0.002	463.26	14.41 ± 0.17	34.8
2358.801 ± 0.010	423.94	6.97 ± 0.17	18.2
2362.782 ± 0.005	423.23	5.86 ± 0.17	15.3
2366.854 ± 0.003	422.50	8.24 ± 0.17	21.4
2015			
1172.340 ± 0.024	852.99	7.92 ± 0.40	9.1
1235.760 ± 0.006	809.22	29.01 ± 0.33	35.4
1299.269 ± 0.021	769.66	8.94 ± 0.63	10.6
1736.429 ± 0.008	575.89	21.68 ± 0.33	26.7
2150.059 ± 0.060	465.10	3.004 ± 0.70	4
2154.861 ± 0.090	464.07	2.06 ± 0.73	4
2158.634 ± 0.011	463.26	17.3 ± 0.3	22.9
2358.722 ± 0.034	423.96	5.501 ± 0.7	8.1

Table 3—Continued

Frequency μHz	Period s	Amplitude mma	Signal/Noise
2362.884 ± 0.023	423.21	8.48 ± 0.70	12.45
2366.742 ± 0.024	422.52	8.11 ± 0.7	11.9

Table 4. List of 15 Periods Used in Fitting GD358 and Corresponding Best Fit Periods.

k	Frequency (μHz)	Period (s)	Uncertainty (s)	Best fit periods (s)
8	2363.318	423.13	0.04	423.12
9	2155.544	463.92	0.04	463.87
10	2007.628	497.83	0.2	493.14
11	1857.716	538.30	0.3	540.80
12	1741.505	574.22	0.1	574.90
13	1619.700	617.40	0.2	615.98
14	1518.160	658.69	0.5	656.61
15	1428.943	699.82	0.2	701.43
16	1369.336	730.28	0.8	741.67
17	1299.147	769.74	0.2	768.84
18	1238.129	807.67	0.2	809.40
19	1170.207	854.55	0.6	854.01
20	1109.271	901.49	0.8	893.00
22	1032.967	968.09	1.4	967.71
24	941.333	1062.32	3.1	1051.16
σ_{rms}				0.964 s
BIC ($n_{\text{obs}} = 15$)				-0.0303 s
BIC ($n_{\text{obs}} = 10$)				0.639 s

Table 5. Master Grid and Best Fit Parameters

	T_{eff} (K)	Mass M_{\odot}	M_{env} $\log(M_*)$	M_{He} $\log(M_*)$	X_o $\log(M_*)$	q_{fm} $\log(M_*)$	
Minimum	21,000	0.500	2.00	4.00	0.10	0.10	
Maximum	30,000	0.700	3.40	7.00	1.00	0.80	
Step size	200	0.010	0.20	0.20	0.10	0.05	
Best fit parameters							
Initial fit	23,600	0.570	−2.00	−5.60	0.50	0.20	4.45 s
Refined fit	23,650.0	0.5706	−2.000 (fixed)	−5.500	0.500	0.195	